UNIVERSITY OF CALIFORNIA SAN DIEGO

Molecular Simulation Frameworks for Mechanistic Investigation of Complex Nanomaterials

A dissertation submitted in partial satisfaction of the
requirements for the degree Doctor of Philosophy

in

NanoEngineering

by

Robert Scanlon Ramji

Committee in charge:

Professor Darren J. Lipomi, Chair
Professor Tod A. Pascal, Co-Chair
Professor Francesco Paesani
Professor Jon Pokorski

2026

The Dissertation of Robert Scanlon Ramji is approved, and it is acceptable in quality and form for publication on microfilm and electronically.

University of California San Diego

2026

TABLE OF CONTENTS

LIST OF FIGURES

LIST OF TABLES

ACKNOWLEDGEMENTS

I will forever be grateful to my committee chair and advisor Dr. Darren Lipomi for his mentorship, support, and the many opportunities he provided to me during my time in his research group. I sincerely thank my committee co-chair and co-advisor Dr. Tod Pascal for encouraging and guiding me as a computational researcher. Both Tod and Darren manifest their kindness, curiosity, and humanity in their research groups, which made both groups a wonderful place to be during my time in graduate school.

This research was made possible by the financial support of the National Science Foundation through the UC San Diego Materials Research Science and Engineering Center (MRSEC, grant DMR-2011924) funding, which supported me as a trainee for the entirety of my enrollment in the Ph.D. program at UC San Diego.

I additionally owe my sincere gratitude to my committee members Dr. Francesco Paesani and Dr. Jon Pokorski for their helpful discussion and input, which helped significantly in making the work presented here more scientifically robust. Thank you also to my many labmates, mentors, mentees, and co-authors who helped me in and out of the lab throughout my journey in the Ph.D. program at UC San Diego.

Chapter 2, in full, is a reprint of the material as it appears in *The Journal of Physical Chemistry B*, 2025. Ramji, Robert S.; Kleinschmidt, Andrew T.; Bhamidipati, Shruti; Zhang, Leon; Chen, Alexander X.; Pascal, Tod A.; Lipomi, Darren J., American Chemical Society, 2025. The dissertation author was the primary investigator and author of this paper.

Chapter 3, in part, has been submitted for publication of the material. Park, Se Young; Lee, Seongjae; Ramji, Robert S.; Yang, Jeehye; Kim, Hyeokjun; Ham, Yoonsang; Park, Myoungjin; Pascal, Tod A.; Lipomi, Darren J.; Kang, Moon Sung. The dissertation author was the primary investigator and author of the computational portions of this material.

Chapter 4, in part, is currently being prepared for submission for publication of the material. Ramji, Robert; Mullooly, Margaret; Duncan, Isla; Brown, William; Lam, Benjamin; Lipomi, Darren J.; Closser, Kristina D.; Jokerst, Jesse V.; Pascal, Tod A. The dissertation author

was the primary investigator and author of this material.

VITA

2020	Bachelor of Science in NanoEngineering, University of California San Diego
2020	Bachelor of Arts in Chinese Studies, University of California San Diego
2026	Doctor of Philosophy in NanoEngineering, University of California San Diego

PUBLICATIONS

Ramji, R. S.; Kleinschmidt, A. T.; Bhamidipati, S.; Zhang, L.; Chen, A. X.; Pascal, T. A.; Lipomi, D. J. "Quantifying the Effect of Intermonomer Improper Angles on Electron Delocalization in Conjugated Polymers." *J. Phys. Chem. B* **2025**, *129*, 7642–7653.

ABSTRACT OF THE DISSERTATION

Molecular Simulation Frameworks for Mechanistic Investigation of Complex Nanomaterials

by

Robert Scanlon Ramji

Doctor of Philosophy in NanoEngineering

University of California San Diego, 2026

Professor Darren J. Lipomi, Chair
Professor Tod A. Pascal, Co-Chair

Fully understanding the behavior of functional nanomaterials requires insight into atomic motion, electron delocalization, bond formation, and interparticle interactions. The resolution required to study these phenomena, particularly under experimentally relevant conditions, often exceeds the capabilities of modern nanocharacterization equipment. Molecular simulation offers a computational microscope with which to investigate these systems at the necessary scale. Yet for many nanomaterial systems of practical interest, the simulation infrastructure needed to gain that insight simply does not exist. This dissertation constructs missing infrastructure across three nanomaterial systems of increasing complexity, enabling mechanistic questions about these

systems to be answered with molecular-scale precision for the first time.

Chapter two considers the smallest system: a single conjugated polymer chain. A method to quantify the effects of intermonomer improper torsion on electron delocalization in conjugated polymers is introduced. Calculations across P3HT, PTB7, and PNDI-T reveal that improper torsion generally disrupts conjugation, though PNDI-T maintains delocalization at significant bending angles due to its extended π-system, suggesting a mechanism by which certain donor-acceptor polymers retain charge transport under strain.

Chapter three scales to molecular behavior influencing a mesoscale network. Photocrosslinking in quantum dot films is modeled using molecular dynamics combined with a Monte Carlo percolation model, achieving quantitative agreement with experimental film retention data. The model reveals the mechanism by which films using ligand-type crosslinkers reach the needed film retention threshold at roughly one-quarter the UV dose of those with additive-type crosslinkers.

Chapter four examines the most complex system: citrate-capped gold nanoparticles functionalized with peptides. A complete simulation framework is developed to measure aggregation free energies across a twelve-peptide series, reproducing the class distinctions observed experimentally and identifying counterion release followed by peptide bridging as the molecular mechanism of assembly.

Together, these projects extend the reach of molecular simulation as a tool for nanoscale characterization, and lay the groundwork for future exploration and development.

Chapter 1

General Introduction and Overview

1.1 Preface

This dissertation presents three computational studies of functional nanomaterials, each addressing a system where the molecular-scale mechanisms governing macroscopic behavior were previously inaccessible to experiment alone. The chapters are organized by increasing system complexity, from a single conjugated polymer chain, to a mesoscale crosslinked nanoparticle network, to a colloidal gold nanoparticle dispersion mediated by peptide interactions. Each study constructs simulation infrastructure that did not exist before this work, enabling mechanistic questions to be answered at atomic resolution for the first time.

The unifying theme is the use of molecular simulation as a characterization tool, and the development of reusable tools and frameworks to allow the extension of the work. Just as electron microscopy extended the reach of structural characterization below the diffraction limit, molecular simulation extends the reach of characterization below the resolution of any physical instrument. The phenomena studied here (electron delocalization, covalent network formation, and interparticle free energy) operate on length and timescales that are simultaneously too small for conventional spectroscopy and too large for routine quantum chemical treatment. Bridging that gap is the central challenge this work addresses.

Each chapter is written to be self-contained, with its own introduction, methods, results, and conclusions. This preface and the sections that follow provide the conceptual and method-

ological background common to all three studies, so that the methods sections in individual chapters may focus on system-specific details rather than first principles.

1.2 Research Motivation and Introduction

Nanomaterials are defined by the dominance of surface and interface effects over bulk behavior, and by the emergence of properties, optical, electronic, mechanical, and chemical, that have no direct analog in macroscopic matter. Understanding and controlling these properties requires knowledge of atomic-scale structure and dynamics. That knowledge is extraordinarily difficult to obtain experimentally. Techniques such as X-ray scattering, electron microscopy, and atomic force microscopy provide structural snapshots, but they do not directly reveal the forces, energies, or dynamic processes that produce those structures.

Molecular simulation fills this gap by providing a physically grounded, fully atomistic picture of nanomaterial behavior. Given a sufficiently accurate model of interatomic interactions, a simulation can, in principle, predict any measurable property and, more importantly, reveal the underlying mechanism responsible for it. The practical value of this approach depends critically on having the right simulation infrastructure for the system of interest: appropriate force fields, model construction pipelines, equilibration protocols, analysis tools, and, where necessary, enhanced sampling methods to access rare events or long timescales.

For many nanomaterial systems of current practical interest, this infrastructure does not exist. The three systems studied in this dissertation each represent a case where the absence of appropriate simulation methods has left central mechanistic questions unanswered. Chapter 2 asks how out-of-plane bending between monomers in a conjugated polymer affects electron delocalization, a question that existing force field methods were not designed to address. Chapter 3 asks why two chemically similar photocrosslinking strategies for quantum dot films differ by a factor of roughly four in their UV dose requirements, a question that requires connecting atomic-scale reaction geometry to macroscopic network connectivity. Chapter 4 asks what molecular

events govern the reversible, peptide-mediated aggregation of gold nanoparticles, a question that requires computing interaction free energies for complex, multi-component colloidal systems.

In each case, answering the mechanistic question required developing new simulation methodology, validating it against available experimental data, and applying it to generate physical insight. The following sections introduce the three computational frameworks common to this work: quantum mechanical methods, molecular dynamics, and Monte Carlo and percolation theory.

1.3 Quantum Mechanical Methods

Quantum mechanics (QM) provides the most accurate available description of interatomic interactions and electronic structure. Its application to nanomaterials problems in this dissertation falls into two categories: direct calculation of energies and electronic properties for small model systems, and the derivation of force field parameters that encode QM accuracy into computationally efficient classical models.

1.3.1 Foundations

The central object in quantum chemistry is the electronic wavefunction, which encodes the probability amplitude for finding each electron at each point in space. The total energy of a molecular system, and all properties derivable from it, follow from solving the time-independent Schrödinger equation. Except for the simplest one-electron systems, this equation cannot be solved exactly. Practical quantum chemistry therefore relies on approximate methods that trade accuracy for computational tractability.

The two principal approximations used in this work are density functional theory (DFT) and second-order Møller-Plesset perturbation theory (MP2). DFT replaces the many-electron wavefunction with the electron density, a scalar field in three dimensions, using the Kohn-Sham framework to map the interacting system onto a set of fictitious non-interacting electrons in an effective potential. The exchange-correlation functional captures all effects not treated exactly;

the choice of functional governs the accuracy and cost of the calculation. MP2 treats electron correlation as a perturbative correction to the Hartree-Fock reference wavefunction, recovering a significant fraction of correlation energy at moderate computational cost.

Both methods require specification of a basis set: a finite set of mathematical functions used to represent the molecular orbitals. Larger basis sets approach the complete basis set limit and generally improve accuracy at greater computational cost. The basis sets used in this work (6-31G*, def2-SVP, 6-311++G**) span a range of sizes appropriate to the different accuracy requirements of each application.

1.3.2 Application to Conjugated Polymer Torsion (Chapter 2)

Chapter 2 requires QM calculations at two levels of theory for distinct purposes. Torsional scans of conjugated polymer dimers, used to characterize how electronic delocalization energy depends on backbone geometry, are performed at the RI-MP2 level. MP2 is appropriate here because it captures the dispersion interactions between π systems that DFT functionals without dispersion corrections can underestimate. For geometry optimizations used to set equilibrium angles in the modified force field, DFT at the BP86/def2-SVP level is sufficient, as these calculations are used only to locate the energy minimum rather than to obtain accurate absolute energetics.

A key methodological challenge in Chapter 2 is isolating the electronic delocalization contribution to the torsional energy from the steric (nonbonded) contribution. The two contributions are not independently observable in a standard QM torsional scan: rotating two monomers simultaneously changes both their conjugation and their van der Waals overlap. The approach taken uses a series of chemically modified dimer structures (a hydrogenated dimer that blocks conjugation, and a methylated monomer that eliminates inter-monomer interactions) to decompose the total energy into components attributable to electronic delocalization and steric interactions separately. All QM calculations were performed using Q-Chem.

Visualization of electronic delocalization in Chapter 2 relies on the anisotropy of the

induced current density (AICD) method, which computes the electronic current density induced by an external magnetic field. AICD isosurfaces provide an intuitive three-dimensional picture of where electrons are delocalized across a molecule, making the abstract concept of π conjugation directly visible as a spatial density. These calculations were performed using Gaussian 16.

1.3.3 Application to Force Field Parameterization (Chapters 3 and 4)

Chapters 3 and 4 use QM primarily to derive partial atomic charges and optimized geometries for use in classical molecular dynamics simulations. Partial charges are obtained using the restrained electrostatic potential (RESP) method, in which the molecular electrostatic potential is computed at the QM level and atomic charges are fitted to reproduce it subject to constraints that enforce chemically reasonable values. In Chapter 3, RESP charges for ligands and crosslinkers are computed at the wB97X-D/6-311++G** level, a range-separated hybrid functional with empirical dispersion corrections that provides accurate electrostatic potentials for organic molecules. In Chapter 4, the same functional and basis set are used for citrate and peptide molecules under implicit solvent conditions.

1.3.4 Basis Sets and Levels of Theory: A Summary

The choice of QM level of theory in each chapter reflects a balance between the accuracy required for the application and the computational cost imposed by the system size. For the small dimers of Chapter 2, MP2 with polarized basis sets is tractable and warranted by the need to accurately resolve small energy differences (less than 1 kcal/mol) between torsional conformers. For the charge derivation tasks in Chapters 3 and 4, DFT with a large basis set is sufficient and provides good electrostatic potentials at reasonable cost. For geometry optimization of conjugated polymer dimers, a smaller basis set (def2-SVP) is acceptable because the objective is identifying the minimum, not characterizing the energy landscape in detail.

1.4 Molecular Dynamics

Molecular dynamics (MD) simulation propagates the positions and velocities of all atoms in a system forward in time by numerically integrating Newton's equations of motion. Given a force field that describes interatomic interactions, MD generates a trajectory from which thermodynamic, structural, and dynamic properties can be computed. MD is the workhorse method of this dissertation, used in all three chapters to equilibrate molecular systems, generate conformational ensembles, simulate chemical reactions (crosslinking), and compute mechanical properties.

1.4.1 Force Fields

A force field is a mathematical model of the potential energy surface of a molecular system, expressed as a sum of terms describing bonded interactions (bond stretching, angle bending, torsional rotation) and non-bonded interactions (van der Waals and electrostatic). The parameters in a force field are fitted to reproduce properties calculated from QM, from experiment, or both.

The bonded and non-bonded functional forms most relevant to this dissertation follow the OPLS, AMBER, and DREIDING conventions. The OPLS framework uses a cosine series to represent torsional potentials and Lennard-Jones 12-6 potential for van der Waals interactions, with geometric mixing rules. AMBER employs a similar functional form but uses Lorentz-Berthelot mixing rules; GAFF (the general AMBER force field) extends AMBER parameters to arbitrary organic molecules and is used for citrate and peptide parameterization in Chapter 4. DREIDING is used for intermolecular ligand-ligand interactions in Chapter 3, where its simple, transferable parameterization is appropriate for describing alkyl chain packing.

Force field accuracy is the dominant source of uncertainty in classical MD simulation. For the conjugated polymer systems in Chapter 2, the inadequacy of standard OPLS parameters for capturing intermonomer torsional energetics is precisely the problem being solved: the existing

force field omits the improper torsion contribution entirely. For the quantum dot systems in Chapter 3, the parameterization of the inorganic core uses a Stillinger-Weber potential developed for II-VI semiconductor materials, while the organic ligand-surface interface requires empirical tuning of Lennard-Jones cross-terms because validated parameters are not available. For the gold nanoparticle systems in Chapter 4, Lennard-Jones parameters for gold are taken from Heinz et al., which accurately reproduce FCC metal surface properties.

1.4.2 Equations of Motion and Thermostats

The equations of motion integrated in all simulations in this dissertation follow the time-reversible, measure-preserving Verlet algorithm derived by Tuckerman et al. This formulation ensures that the integration scheme preserves the phase space volume defined by the extended Hamiltonian, which is essential for producing correct statistical mechanical averages.

Temperature control in NVT (constant number, volume, temperature) and NPT (constant number, pressure, temperature) ensembles is achieved using a Nosé-Hoover thermostat, which introduces a fictitious degree of freedom coupled to the kinetic energy of the system. Pressure control in NPT simulations uses either an Andersen barostat (Chapter 3) or is implicit in the isochoric simulation setup (Chapter 4). All simulations are performed using LAMMPS (Large-scale Atomic/Massively Parallel Simulator).

1.4.3 Enhanced Sampling: Steered Molecular Dynamics and Umbrella Sampling

Standard MD simulation explores only the region of configuration space accessible within the simulation time, which for systems with high energy barriers may be far from the full Boltzmann distribution. Chapter 4 requires computing the free energy profile (potential of mean force, PMF) for separating two gold nanoparticles from contact to large separation, a process that involves crossing barriers far larger than the available thermal energy.

Steered molecular dynamics (SMD) addresses this by applying a moving harmonic

restraint to the collective variable of interest (here, the inter-nanoparticle center-of-mass distance), driving the system along a reaction coordinate while recording the force required at each point. The work performed against this force, accumulated over many independent pulling trajectories, in principle yields the free energy difference between states via the Jarzynski equality:

$$e^{-\beta \Delta F} = \left\langle e^{-\beta W} \right\rangle, \tag{1.1}$$

where $\beta = 1/(k_B T)$, ΔF is the free energy difference, and W is the irreversible work performed in each trajectory. The angle brackets denote an average over independent non-equilibrium realizations of the process.

In practice, the exponential average in Equation 1.1 is dominated by rare low-work trajectories, and when dissipation is comparable to the free energy difference itself, a feasible number of realizations cannot sample them. This is precisely the regime of the nanoparticle pulls in Chapter 4. That chapter therefore adopts the symmetric bidirectional estimator, the Gaussian-work limit of the Crooks fluctuation theorem[1] and of the Bennett acceptance ratio,[2] in which the free energy is the half-difference of the mean work measured on compression and expansion legs, $\Delta F = (\langle W_{\text{push}} \rangle - \langle W_{\text{pull}} \rangle)/2$, and the frictional contribution cancels by symmetry rather than by exponential reweighting. SMD is implemented in Chapter 4 using the PLUMED 2 plugin interfaced with LAMMPS, applying push-pull cycles that drive the nanoparticles through repeated contact and separation.

Umbrella sampling[3] provides a complementary, fully equilibrium route to the same free energy profile. Rather than driving the system along the coordinate, a series of static harmonic restraints confines independent simulations to overlapping windows spanning the coordinate, and the biased distributions sampled in each window are recombined into an unbiased profile using the weighted histogram analysis method (WHAM)[4] or its binless generalization, the multistate Bennett acceptance ratio (MBAR).[5] Because umbrella sampling shares no machinery with the nonequilibrium estimator beyond the force field and the coordinate, agreement between the two

constitutes a genuine cross-validation, and Chapter 4 uses it in that role.

1.4.4 Crosslinking Simulations

Chapter 3 requires a non-standard MD application: simulating the progressive formation of covalent bonds during UV-induced photocrosslinking. Standard MD force fields treat bonded topology as fixed; crosslinking requires dynamically modifying the topology during the simulation to reflect newly formed bonds.

The protocol adopted in Chapter 3 implements crosslinking iteratively. In each cycle, the system is equilibrated, and reactive contacts (atom pairs within a specified cutoff distance meeting the criteria for bond formation) are identified. The geometrically closest contact is selected, the bond is formed by modifying the topology (adding a C-C bond and transferring a hydrogen to the benzophenone oxygen, faithfully representing the ketyl-radical mechanism), and the cycle repeats. This iterative approach captures the progressive nature of the crosslinking reaction and produces structurally realistic crosslinked networks without requiring explicit simulation of radical chemistry.

1.4.5 Stress-Strain Simulations

Chapter 3 also employs tensile deformation simulations to characterize the mechanical stiffness of crosslinked quantum dot films. In these simulations, the simulation box is stretched along one dimension at a constant rate while the resulting stress (force per unit area, computed from the virial pressure tensor) is recorded as a function of strain. Although the strain rates accessible in MD (roughly nanometers per nanosecond) far exceed those achievable experimentally, the relative stiffness between systems, and the qualitative shape of the stress-strain curve, are meaningful and interpretable. This approach follows established practice for comparative MD mechanical studies.

1.5 Monte Carlo and Percolation Theory

Monte Carlo (MC) methods use random sampling to estimate properties that are analytically intractable. The name refers to the use of random numbers, after the Monte Carlo casino.

Percolation theory studies the conditions under which a connected cluster spanning an entire system can form from randomly distributed local connections. The canonical model is bond percolation on a lattice: each bond between adjacent lattice sites is present independently with probability p. Below a critical threshold p_c (the percolation threshold), all clusters are finite and no spanning cluster exists. Above p_c, a spanning cluster appears and grows with increasing p. At p_c itself, the cluster size distribution exhibits a power-law form characteristic of a continuous phase transition.

The percolation threshold depends on the lattice geometry and dimensionality. For the three-dimensional hexagonal close-packed (HCP) lattice, which is an appropriate model for close-packed colloidal films, the critical bond probability is approximately $p_c = 0.12$. This value represents the minimum fraction of nearest-neighbor bonds that must be present for macroscopic connectivity.

1.5.1 Application to Quantum Dot Film Crosslinking (Chapter 3)

Chapter 3 uses Monte Carlo bond percolation simulations to connect the local crosslinking probability computed from atomistic MD simulations to the macroscopic connectivity of crosslinked quantum dot films. The relevant quantity for film performance in photolithographic patterning is not simply percolation (the existence of a spanning cluster) but rather a practical threshold: the fraction of UV dose required to connect 95% of all nodes in the film, which corresponds to the experimentally observed film retention ratio of greater than 0.95 after development.

The MC percolation simulations are implemented on model HCP lattices representing the colloidal QD array. Each lattice node represents a QD, and each bond is present with probability

p, which is taken directly from the atomistic crosslinking simulations as the nearest-neighbor bond probability (the fraction of neighboring QD pairs connected by at least one bridging crosslink). By sweeping p across its range and measuring the resulting connected fraction, the simulations determine the value of p required to achieve 95% macroscopic connectivity: $p_{95} = 0.31$ for the film geometry studied.

This value of p_{95} serves as the critical target for both crosslinker types. Because the atomistic simulations show that the ligand-type crosslinker reaches $p = 0.31$ after reacting far fewer benzophenone groups than the additive-type crosslinker, the percolation model directly predicts the observed fourfold difference in required UV dose. The MC approach thus functions as the quantitative bridge between molecular-scale simulation results and macroscopic experimental observables.

1.5.2 Validation

The MC percolation implementation was validated by computing the percolation threshold for a $10 \times 10 \times 10$ cubic HCP lattice and comparing it to the published theoretical value of approximately 0.12. The agreement between the simulated and theoretical thresholds confirms that the implementation is correct and that finite-size effects are negligible at this lattice size for the purposes of threshold estimation. Simulations on a film geometry lattice ($50 \times 50 \times 3$) yielded the same p_{95} value as the bulk lattice, indicating that the 95% connectivity threshold is insensitive to the lateral-to-thickness aspect ratio at the dimensions studied here.

Chapter 2

Quantifying the Effect of Intermonomer Improper Angles on Electron Delocalization in Conjugated Polymers

Robert S. Ramji, Andrew T. Kleinschmidt, Shruti Bhamidipati, Leon Zhang, Alexander X. Chen, Tod A. Pascal, and Darren J. Lipomi. Quantifying the Effect of Intermonomer Improper Angles on Electron Delocalization in Conjugated Polymers. *J. Phys. Chem. B* **2025**, *129*, 7642–7653. DOI: 10.1021/acs.jpcb.5c02849

2.1 Abstract

Electron delocalization between monomers in conjugated polymers influences both the charge transport and the mechanical properties of this class of materials. While this delocalization is generally understood to be maximized by coplanar monomer arrangements that enable π-orbital overlap, the precise geometric factors controlling delocalization remain incompletely characterized. Current molecular mechanics (MM) models of conjugated polymers primarily focus on intermonomer dihedral torsion, neglecting the potential effects of out-of-plane ("improper") torsion between monomers. Here, we develop a method to isolate and quantify improper dihedral torsion effects on the electronic structure of dimer or donor–acceptor unit structures for three representative polymers: P3HT, PTB7, and PNDI-T. Quantum mechanical calculations reveal that improper torsion generally disrupts electronic delocalization, though PNDI-T maintains significant conjugation even at improper angles up to 30°, likely due to its

extended π-system. While coupling between improper and dihedral torsion is observed, the energetic effects appear to be minimal ($<$1 kcal/mol) under typical conditions. These findings suggest that existing MM models may safely omit improper torsion parameters for simulations of local structures and motivates future studies aimed at quantifying its effect on larger-scale polymer films. Finally, to aid interpretation of these results, we have developed an interactive visualization tool that simultaneously displays delocalization energy profiles and 3D electron density isosurfaces.

2.2 Introduction

π-Conjugated polymers are characterized by a motif of alternating double and single bonds along the backbone. In this arrangement, electrons may delocalize from the bonding orbitals from which they originate. This delocalization of electrons along the backbones of conjugated polymers gives rise to an optical bandgap and semiconducting behavior.[6–8] Delocalization is energetically favorable and usually depends on the degree of alignment between the π-bonds in the backbone, with notable exceptions for certain monomer selections.[9] A planar conformation of sequential bonds maximizes this overlap, while deviations from planarity reduce it. Thus, electronic delocalization acts as a driving force toward the coplanar configuration of monomers.[10] As a consequence of this drive toward coplanarity, conjugated polymers tend to be more rigid than saturated polymers.[11,12] This relationship between electronic structure, optoelectronic properties, and the mechanical flexibility of conjugated polymers has motivated a number of studies focusing on understanding and accurately modeling intermonomer rigidity in conjugated systems.[13,14]

Part of the motivation for computational studies is that the backbone planarity of a conjugated polymer is difficult to measure experimentally.[15] In these studies, it is typical to compute the energy as a function of the proper dihedral torsional angle between monomers. Hereon, the term “dihedral torsion” will be used to refer to intermonomer proper dihedral torsion,

i.e., a 'twisting' angle between two conjugated monomers about the connecting bond. Dihedral torsion can be likened to the spinning of a revolving door, where the degree of rotation around the central axis corresponds to the torsion angle between atoms in the molecule. However, deviation from planarity between monomers can also occur through improper dihedral torsions. These intermonomer improper dihedral torsions occur when the motion of the polymer produces an out-of-plane 'bending' between monomers. This motion occurs in the direction of the normal vector relative to the orientation of the conjugated ring. Improper torsion can be likened to the motion of a door hinge, with the center of mass of one monomer moving as the torsional angle increases. In this work, we will simply refer to intermonomer improper dihedral torsion as "improper torsion".

Both dihedral and improper torsion can break the planarity of conjugated polymer backbones; however, research has historically focused on dihedral torsion.[14,16] One widely applied technique for characterizing the drive toward coplanarity between adjacent monomers of a conjugated polymer is the torsional scan.[17–19] In this method, the energy of a simple oligomer, such as a dimer, is calculated using quantum mechanics (QM) at planarity. Then, the dihedral angle between monomers is scanned at a set increment (often 10°) from planarity (0°) to 180 or 360°. At each step, the energy of the molecule is calculated. This progressive increase in intermonomer torsion interrupts electron delocalization across the backbone, and usually peaks when the monomers are perpendicular to each other at 90°. Interruption of delocalization is energetically unfavorable, and constitutes a significant component of the potential energy profile of a torsional scan.[10] The resulting torsional energy profile over the intermonomer dihedral can be used to fit molecular mechanics (MM) force field (FF) parameters for large-scale molecular dynamics (MD) simulations. This profile defines the energy of deplanarization (i.e., how rigid the polymer is).

The torsional scan method characterizes the energy of one type of torsion, i.e., the conventional dihedral torsion.[15] However, it is well-known that semiconducting polymers can also experience improper torsion between monomers. Like dihedral torsion, improper backbone

torsion disrupts coplanarity and limits π-orbital overlap. Improper torsion and dihedral torsion can also occur simultaneously; given the dependence of electron delocalization on backbone geometry, it follows that these effects must influence the energetic barriers to both dihedral and improper torsion. However, even basic investigation of improper torsion at the QM level is beyond the coverage of current literature for organic semiconductors.[14] As a result, the energy of dihedral torsion cannot be decoupled from the energy of improper torsion in a conventional torsional scan.

Recent advances in organic electronics have challenged conventional wisdom about torsional effects, that is, materials with large dihedral twists, which were expected to show low mobilities, have demonstrated excellent performance in some cases.[20,21] These findings suggest that understanding of torsional effects is incomplete, especially with respect to the role of improper torsion. However, isolating the effects of improper torsion is challenging. Clashes that arise between atoms of the involved monomers lead to very large energy penalties, even at low degrees of improper torsion. In these cases, it can be hard to separate these nonbonded effects from the underlying covalent energies using conventional methods. An additional difficulty arises from the expected correlation between the energetics of improper torsion and those of dihedral torsion. Due to this coupling, it is not possible to fully characterize the energetics stemming from improper torsion using a simple modification of angular or improper potentials. As a result, current models of improper torsion rely on terms taken from a general force field (i.e., OPLS, CHARMM, GAFF), and are focused on maintaining the rigidity of aromatic rings rather than considering intermonomer effects.[22–24]

Here, we present a comprehensive framework for modeling and separately quantifying the effects of proper and improper dihedral torsion in conjugated polymer repeat units. We applied this framework to a set of conjugated dimers and donor–acceptor units to characterize the relationship between electron delocalization and intermonomer backbone conformation. We used the electron delocalization data to create custom force field parameters that model the coupled improper–proper dihedral energy effects to evaluate potential accuracy gains in MM models

of these materials. Additionally, we developed an interactive visualization tool that integrates molecular geometries, delocalized electron density distributions, and energy profiles.

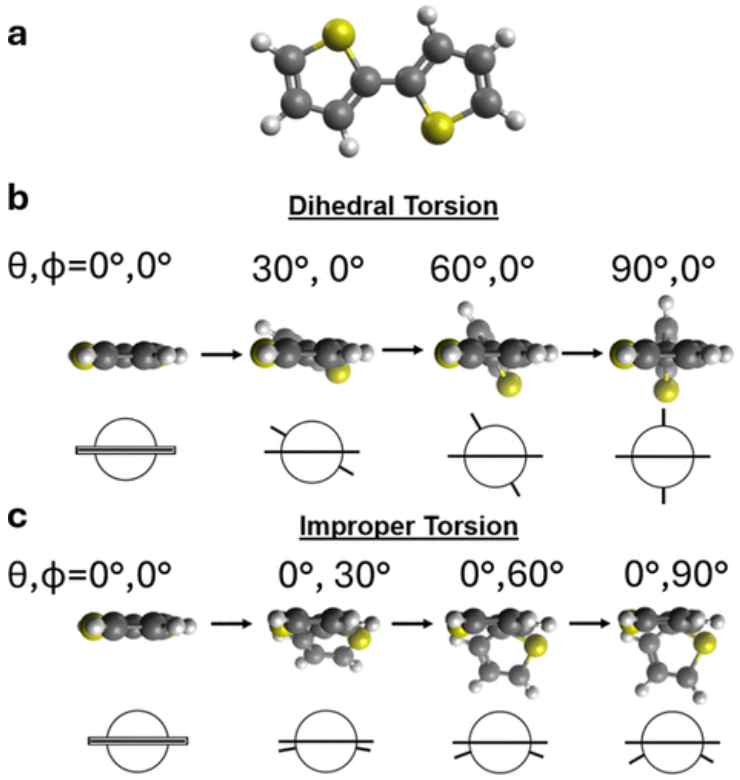

Figure 2.1. Improper vs proper intermonomer dihedral torsion in conjugated polymers. Conjugated polymers can experience two types of torsion: proper dihedral torsion and improper dihedral torsion. θ is hereon used to refer to the proper dihedral torsional angle, and ϕ to the improper dihedral torsional angle. (a) Model conjugated dimer (bithiophene) in a coplanar geometry. In (b) dihedral torsion, the twisting of monomers does not result in a change in the center of mass of the monomers. This is in contrast to (c) improper torsion, in which an increase in the degree of bending accordingly shifts the center of mass of one monomer.

2.3 Methods

To extract the energies arising from improper torsion between two aromatic monomer residues, we extended a previously reported methodology.[10] This prior work introduced a method that uses a series of QM energy calculations to produce highly accurate parameters for proper dihedral backbone torsions. The torsional potential can be attributed to two primary components: (1) steric/nonbonded interactions and (2) covalent electronic effects. Since steric contributions,

which often drive monomers away from planarity, are already accounted for in molecular mechanics models through nonbonded force field terms (van der Waals and electrostatic interactions), the methodology isolates these effects to prevent double-counting. This enables a potential solely associated with covalent delocalization interactions to be obtained. Relying on QM calculations alone allows the planarizing energy of electron delocalization to be decoupled from steric interactions.[10] We expand upon this method in the present work, where scans through a combined set of dihedral and improper angles are used to derive a coupled improper–proper (CIP) potential.

To isolate the energy related to nonbonded interactions, we used a three-step process (Figure 2.2). First, a set of torsional scans were conducted on an unmodified dimer starting from the coplanar structure. We generated a set of dimer structures with varying degrees of improper torsion, in increments of 5° from 0 to 30°, and in larger increments of 10° from 30 to 60°. We then performed a torsional scan of the intermonomer dihedral on each of these starting structures in increments of 10°, from 0 to 360°. For the second step, this process was repeated by conducting an identical set of scans with a hydrogenated dimer structure, where two hydrogen atoms were added to one of the monomers to block electron delocalization. For the third step, this process was repeated with another structural variant, in which one of the rings was replaced with a methyl group (a "methylated monomer"). The nonbonded energy (i.e., steric forces) was isolated by subtracting the energy associated with conjugation (determined using the methylated monomer) from the energy of the hydrogenated dimer. The energy associated with electronic delocalization can be isolated by subtracting the calculated energy of the hydrogenated dimer from the energy of the simple dimer. After running the full set of scans for the given dimer, a unique set of OPLS-style dihedral parameters was fitted to the data produced by each of the torsional scans.[22] This set of dihedral parameters was subsequently incorporated into a specialized force field using PLUMED to couple the improper and dihedral torsional angles.[25]

To determine the effectiveness of our method across a diverse array of π-conjugated polymers, we tested three representative polymers: poly(3-alkylthiophene) (P3HT), polythieno[3,4-

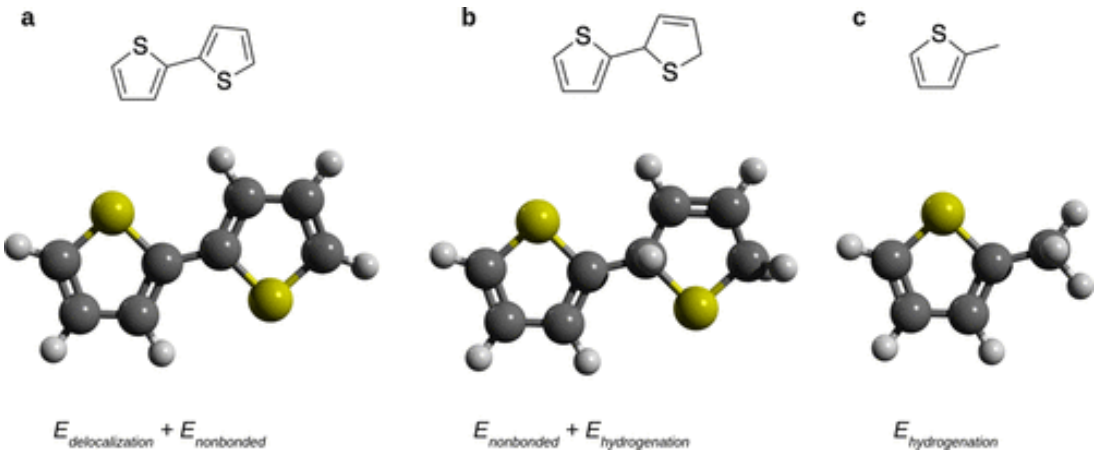

Figure 2.2. Method of isolating the energy associated with electronic delocalization. Torsional scans were conducted on (a) a standard dimer, (b) a hydrogenated dimer, and (c) a methylated monomer (i.e., where one monomer is replaced by a methyl group). By subtracting the calculated energy (relative to improper angle) of the hydrogenated dimer from the simple dimer, the delocalization energy can be isolated. Similarly, by subtracting the calculated energy of the methylated monomer from the hydrogenated dimer, the nonbonded energy can be isolated. Thus, this method allows one to decouple the energies related to electronic delocalization and steric forces.

b]-thiophene-co-benzodithiophene (PTB7), and poly(naphthalene diimide) with a single bridging thiophene (PNDI-T). P3HT, a well-studied homopolymer, is often used as a model for semiconducting polymers.[26] PTB7 was selected for its benzodithiophene residue, which is common in p-type donor–acceptor (D–A) polymers.[13] Additionally, PTB7 offers the opportunity to investigate the effects of distinct regiochemical couplings within the monomer: an outward-pointing fluorine ("F-out" configuration) and inward-oriented fluorine ("F-in" configuration). Finally, PNDI-T was chosen because the naphthalene diimide backbone motif is common for n-type D–A polymers. PNDI-T is highly sterically hindered in the planar state, causing it to adopt a twisted conformation,[18] and its monomers have much greater differences in electronegativity compared to PTB7. For computational efficiency and to focus on backbone conjugation, all polymers were modeled with methyl groups substituting the side-chains or R-groups.

To determine the relative accuracy of the method described above, we compare it to both a conventional parametrization (general OPLS force field parameters from LigParGen)

and to our previously reported delocalization energy parametrization. We generated a randomly sampled set of dimer structures with varying improper and dihedral torsions, where all other internal degrees of freedom were restricted using the RIGID package in LAMMPS.[27] OPLS FF parameters were applied to the dimers using LigParGen.[28] All torsional parameters were set to zero and the simulation was performed at 800 K to allow the dimer to twist and bend freely, allowing the full conformational space to be sampled. Snapshots of random conformations were taken every 100 ps. Quantum calculations were conducted for each conformation at the RI-MP2 level for a total of 100 conformations using QChem 5.4.[29] These QM-calculated energies were used to compute the difference in energy between each sampled dimer conformation and the coplanar conformation. We then compared: (1) a conventional dihedral parametrization, (2) our previously reported delocalization energy-based MM parameters, and (3) a new, specialized force field coupling dihedral and improper torsion.[25]

To assess the effect of improper torsions in polymer films, we performed MD simulations using a standard version and our modified version of the OPLS FF for the three model conjugated polymers. For the default FF, we used the standard OPLS-style force fields obtained from LigParGen.[28,30,31] In the modified style, the parameters from LigParGen were used again, but the equilibrium intermonomer angles were changed to the optimal angle as determined by a geometry optimization using density functional theory (DFT) at the BP86/def2-SVP level, shown by Matt et al. to produce accurate interplanar angles between conjugated moieties.[32] Initial conformations of the polymer film were obtained from Packmol[33] at a density of approximately 0.2 g/cm^3. We then performed a quench-annealing MD protocol to equilibrate our films using LAMMPS.[34] The van der Waals and real space Coulomb cutoffs were set to 10 Å. The reciprocal space Coulomb interactions were computed with a particle–particle particle–mesh solver, with an error tolerance of 10^{-6}.[35] Each MD simulation was initiated with 500 conjugated gradient steps, followed by gradual heating to 300 K over 0.5 ns. This was followed by simulations in the NPT ensemble for 5 ns at 400 K, before being cooled to 300 K over 0.5 ns. During NPT, we used the time-reversible measure-preserving Verlet integrators derived by Tuckerman et al.[36] for

the time integration. Finally, NVT production dynamics ran at 300 K for 1 ns, during which the improper angles were sampled.

To make the communication of quantitative results more visually intuitive, we developed an interactive web application to visualize the relationship between molecular structures and electron delocalization patterns. For each of the molecular conformers studied, we calculated the delocalized electron density using the "anisotropy of the induced current density" (AICD) method.[37] This calculation required first identifying the π-bonding molecular orbitals (MOs) for each conformer. We performed a population analysis on each structure using Gaussian.[38] We then developed a systematic approach using a scoring algorithm that evaluated two key criteria: (1) the alignment of orbital density relative to molecular bond vectors, and (2) the energy level of the orbital; this approach builds on methods developed by Lu and Chen.[39] For each conformer, we selected the highest-scoring MOs for AICD analysis, which generated three-dimensional isosurfaces representing the delocalized electron density. All Gaussian calculations were performed using the Hartree–Fock method with a 6–31G* basis set. These isosurfaces are interactively displayed over the molecular structures in our web application, allowing users to examine spatial relationships between molecular geometry and electron delocalization patterns.

2.4 Results and Discussion

We determined the distribution of intermonomer improper angles for P3HT, PTB7, and PNDI-T using two angular parametrization methods (Figure 2.4). Surprisingly, the distributions of improper angles were statistically similar for all three polymers, across both angular parametrization methods. This gives rise to two important results. First, our simulations suggest that most conjugated polymer films will have some degree of improper torsion, regardless of how the intermonomer angles are parametrized. The means of the distributions were all around 4°, while the probability of observing an improper torsional angle of 0° was very low (between 2.0 and 3.8%). Second, significant improper angles occur in all conjugated polymers. The

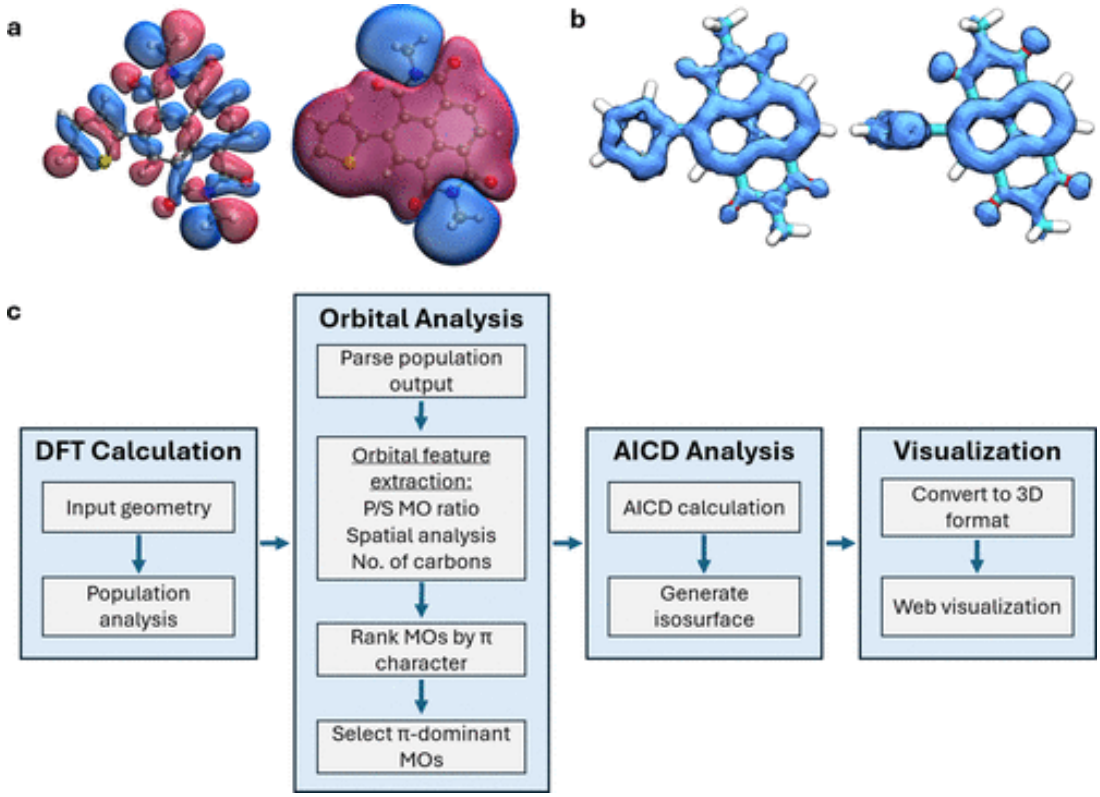

Figure 2.3. Motivation and protocol for obtaining AICD isosurfaces for conjugated polymers. (a) Shows examples of molecular orbitals of PNDI-T with low and high π-bonding characters. (b) Displays AICD isosurfaces of PNDI-T π-bonding MOs for 0° coplanar and 90° orthogonal conformations. (c) Describes the protocol used to generate the π-MO AICD isosurfaces for the conjugated dimers examined in this study.

probability of observing large improper angles between monomers (i.e., 8° or greater) occurs at least as often as the near-coplanar conformation (improper angle <2°), on average 15% vs 12% respectively. Thus, we conclude that improper torsion may be an important contributor to the overall energetics of conjugated polymer chains, and should be explicitly considered in force field parametrizations for systems where its energetic impact is determined to be significant.

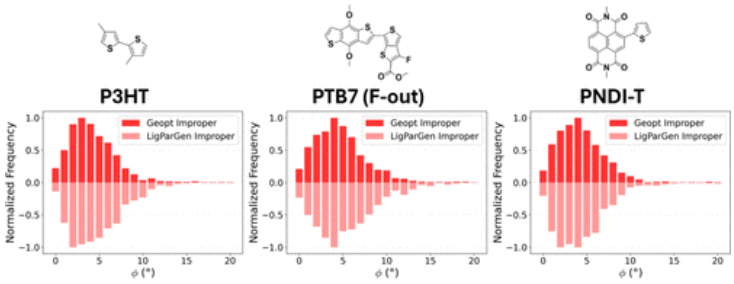

Figure 2.4. Comparison of improper angle populations in different angular parametrizations. Mirror histograms displaying improper angles of randomized polymer films with different angular configurations. In the LigParGen parametrization (light red, mirrored to negative values), the angular parameters were taken from an OPLS parametrization of the conjugated dimer. In the Geometry-Optimized parametrization (dark red, positive values), the angles were set to their equilibrium positions in a quantum mechanical geometry optimization. While geometry optimization was expected to lead to less improper torsion, both methods show modest amounts of improper torsion.

When dihedral torsion (proper or improper) is induced on a dimer, the energy of the system changes relative to the torsional effect on nonbonded interactions and electronic delocalization. We first investigated the effect of coupled dihedral and improper torsion on P3HT, PTB7, and PNDI-T using conventional torsional scans (Figure 2.5). For all polymers, overall energetic differences are dominated by a dramatic increase in steric energy at high degrees of improper torsion. Our simulations also indicate that certain combinations of dihedral and improper torsion can reduce the relative strength of steric clash compared to the 0° improper conformation. In P3HT, the energy of adjacent monomers increases sharply and decreases near 0° of dihedral torsion as the large sulfur atom becomes close to the hydrogen atoms in the adjacent ring. For PNDI-T, there is a clear potential energy maximum at 180°, a barrier over 3 times higher than the next largest local maximum, and no clear energetic minima because all conformations suffer

from steric hindrance.

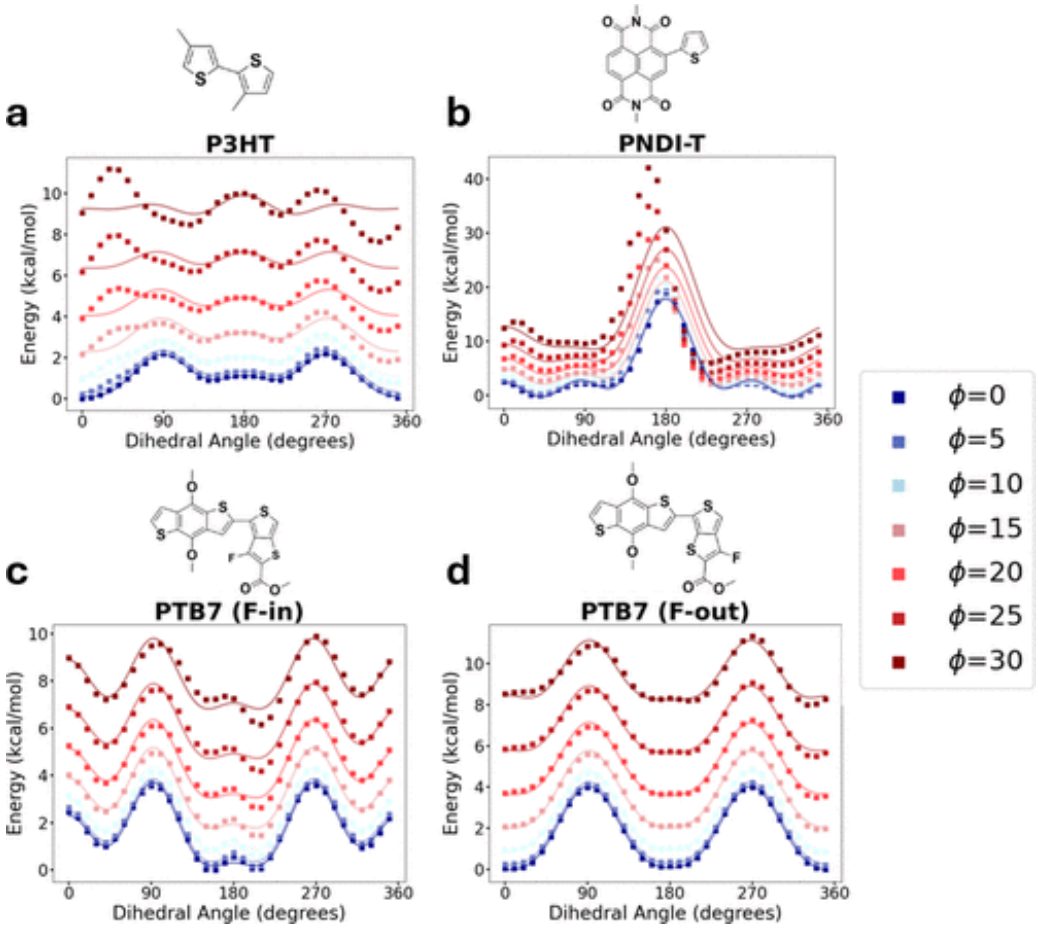

Figure 2.5. Total energy from QM proper-improper torsional scans. Energy calculated directly from QM torsional scans of adjacent monomers for (a) P3HT, (b) PNDI-T, (c) PTB7 F-in and (d) PTB7 F-out relative to dihedral angle (from 0 to 360°) and improper angle (from 0° in blue to 30° in red). Scatter plot points are data, solid lines are OPLS dihedral fits.

These standard QM scans reveal that increased improper torsion significantly distorts the proper dihedral profile due to steric clashes between monomers. Since nonbonded interactions dominate these profiles, they cannot be directly used for parameter fitting. By isolating the delocalization energy (removing nonbonded components), we can successfully fit OPLS dihedral parameters, and understand how improper and dihedral torsion affect the drive toward coplanarity in conjugated polymers (Figure 2.6).

The delocalization energy profiles (without nonbonded forces) are similar for both PTB7

configurations (Figure 2.6), indicating that fluorine placement minimally impacts the intrinsic electronic preference for planarity. However, when nonbonded forces are included, the energy profiles differ substantially, revealing that steric effects from fluorine positioning, not changes in electronic delocalization, drive the observed conformational differences.

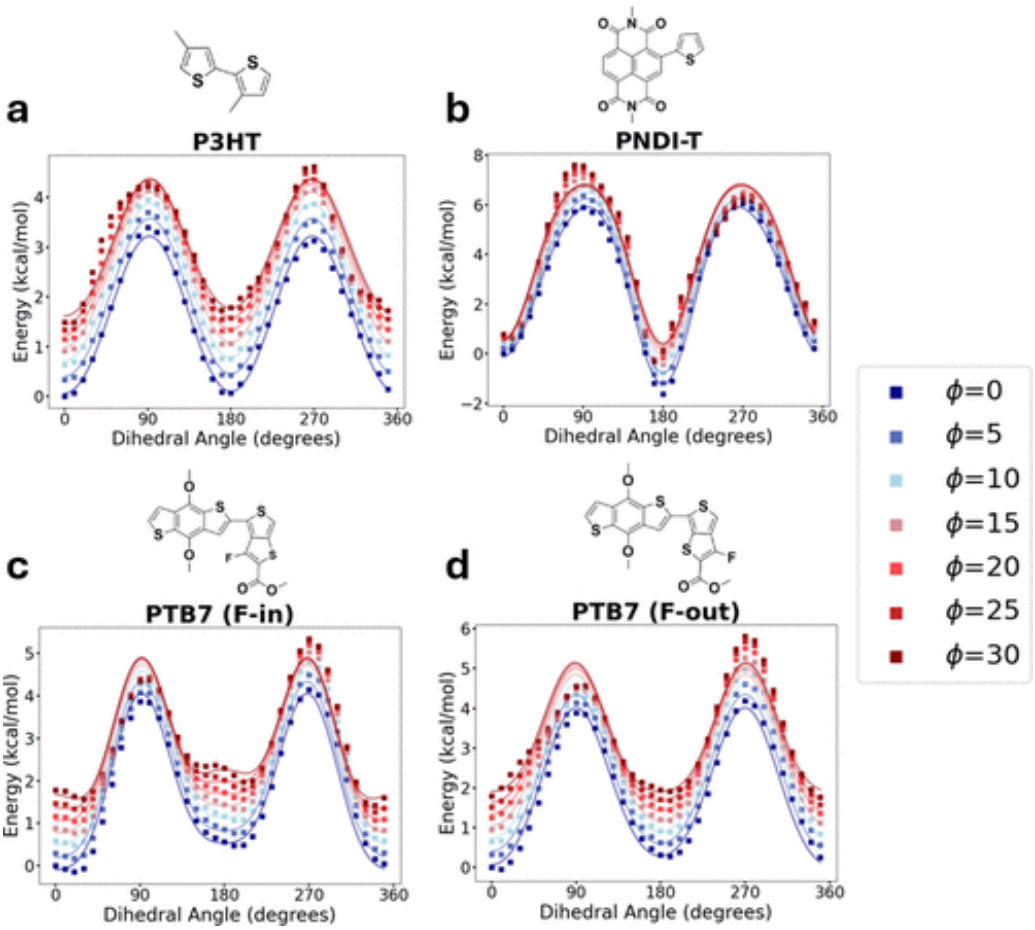

Figure 2.6. Isolated delocalization energy from QM for proper-improper torsional scans. Energy associated with electronic delocalization for (a) P3HT, (b) PNDI-T, (c) PTB7 F-in and (d) PTB7 F-out relative to dihedral angle (from 0 to 360°) and improper angle (from 0° in blue to 30° in red). Scatter plot points are data, solid lines are OPLS dihedral fits. By removing the nonbonded energy (e.g., steric interactions) from each simulation, the effect of both dihedral torsion and improper torsion on the delocalization energetics can be elucidated.

Once the nonbonded energies are removed, it becomes evident that the potential barrier associated with dihedral torsion tends to decrease slightly as improper torsion increases in P3HT and in PTB7. For all three polymers, there are energetic minima around dihedral angles near 0

and 180°, and maxima around 90 and 270°. For P3HT and PTB7, an increase in improper torsion decreases the height of the torsional barrier by ∼0.33 kcal/mol for P3HT and ∼0.78 kcal/mol for PTB7. This indicates that increasing improper torsion impedes intermonomer conjugation, which reduces the total amount of energy associated with electronic delocalization available to be gained or lost.

Conversely, PNDI-T shows a comparatively small resistance to improper torsion and a slight increase in the torsional barrier of ∼0.27 kcal/mol (Figure 2.7a). This finding indicates that electron delocalization is not significantly obstructed, and may even be enhanced by improper torsion in this polymer, likely due to the large π-electron system of the naphthalene diimide monomer. This finding offers a suggestion as to why poly(naphthalene diimide)-based polymers, which exhibit substantial degrees of backbone disorder, can maintain good electronic properties under large strains (e.g., in stretchable OFET devices).[40,41]

For P3HT and PTB7, the barriers to improper torsion are more than double the respective barrier to dihedral torsion at low angles (Figure 2.7b), meaning more pathways for electronic delocalization are broken than are created. Our simulations of PNDI-T suggest that favorable delocalization energetics can be maintained despite a disordered backbone. Future work is needed to determine if and when improper torsion makes more conjugation than it breaks, whether improper torsion allows for additional overlap within the π-system, thus maintaining conjugation over larger length scales.

We obtained energies for a range of dimer conformations using the coupled proper-improper parametrization method and calculated the errors with respect to energies obtained from QM. We compared these errors to those of two reference models to assess the impact of the new parametrization method on the accuracy of the molecular mechanics model (Table 2.1). The improved parametrization enhanced accuracy compared to conventional force fields across all studied polymers. However, the improvements were modest in comparison to our previous OPLS-DE parametrization method. This suggests that while incorporating coupling effects between proper and improper dihedral torsions in conjugated polymer models does increase accuracy, the

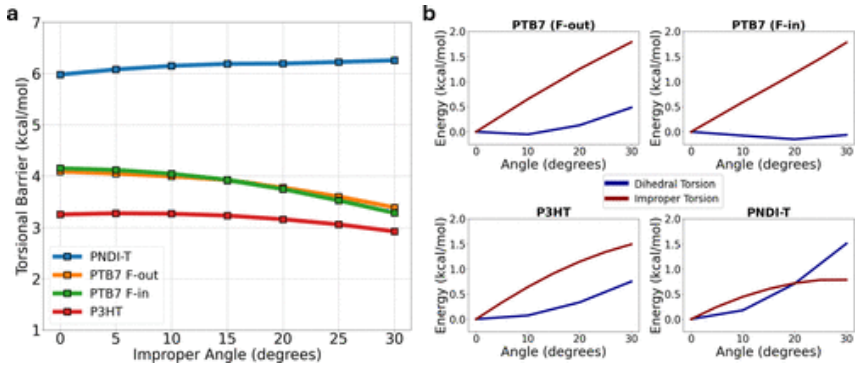

Figure 2.7. Delocalization energy barriers to proper and improper torsion. (a) Barriers to proper dihedral torsion as a function of improper angle for each of the polymers studied. The torsional barrier decreases slightly relative to increasing improper torsion for P3HT, PTB7 (F-in and F-out), but changes little for PNDI-T. (b) Energy with respect to isolated dihedral torsion and improper torsion for each of the polymers studied. For P3HT and both PTB7 variants, increasing the improper angle has a much higher energetic cost compared to dihedral torsion. This does not hold true for PNDI-T, which possesses a much larger conjugated structure compared to the other polymers.

majority of improvements over conventional models stem from better parametrization of proper dihedral torsions.

Table 2.1. Mean error reductions achieved using the coupled improper–dihedral parametrization, relative to a conventional OPLS parametrization and to the previously reported OPLS-DE delocalization energy parametrization. Error is the difference between the molecular mechanics energy and the reference QM energy (aug-cc-pVTZ RI-MP2), averaged across a comprehensive set of randomly sampled conformers. Negative values indicate reduced error.

Polymer	Mean error change vs conventional (kcal/mol)	Mean error change vs delocalization (kcal/mol)
P3HT	−0.54	−0.23
PTB7 F-out	−0.11	−0.03
PTB7 F-in	−0.62	−0.29
PNDI-T	−1.12	−0.04

After developing the computational framework necessary to quantitatively investigate the relationship between electron delocalization and backbone conformation, we identified a gap in our ability to effectively visualize and communicate these results. To address this limitation, we developed an interactive web application (Figure 2.8a) to facilitate exploration

of electron delocalization in conjugated polymers. Several alternative methods have been proposed to visualize electron delocalization, including natural bond orbital (NBO) analysis,[42] electrostatic potential (ESP) mapping, and electron localization function (ELF) calculations.[43–47] However, most of these techniques are optimized for planar, aromatic systems and have limited applicability to nonaromatic or nonplanar conjugated polymers.[37,39] We identified the anisotropic induced current density (AICD) method as a promising alternative for visualizing π-electron delocalization in conjugated polymers.[37] The advantage of AICD lies in its ability to capture current density distributions induced by external magnetic fields that are independent from the underlying electron density. AICD isosurfaces thus provide an intuitive representation of electron delocalization beyond conventional depictions. Additionally, we implemented a conversion method to render these representations in an interactive 3D format. These visualizations not only improve our understanding of these systems but also serve as a valuable tool for broader dissemination of insights into conjugated polymer behavior.

2.5 Conclusion

This work sought to understand the effect of improper torsion on the energetics of three model polymers: P3HT, PTB7, and PNDI-T. Our simulations suggest that varying degrees of improper torsion would be common in the polymer chains that compose a solid sample. Improper torsion decreases electron delocalization when planarity is broken, but can increase electronic delocalization if additional overlapping of the π-orbitals is induced. In general, we find that the first effect is stronger than the second, and thus an increase in improper torsion generally results in a greater energetic barrier to torsion for all polymers here except PNDI-T. As a result, improper torsion is generally an obstacle for electronic delocalization.

Additionally, we find that energetic penalties from steric interactions obscure the energetic penalties associated with electronic delocalization relative to increasing improper torsion. By modifying our computational method to isolate the energy related to electronic delocalization, we

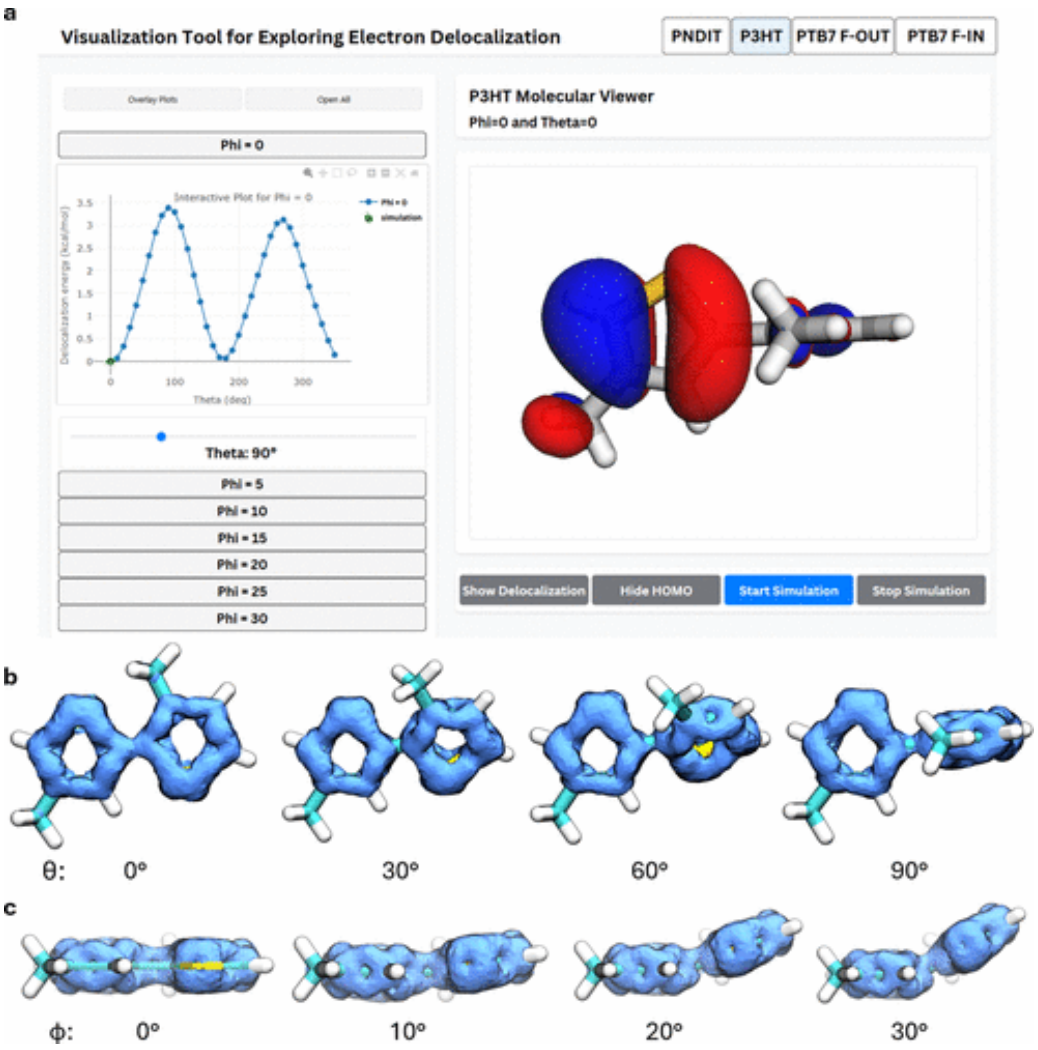

Figure 2.8. Interactive web application design and delocalization isosurface examples. (a) An interactive web application for exploring the 3D structure of conjugated dimer conformers, their delocalization energy, HOMO density plots, and associated delocalized electron density maps. Delocalized electron density (AICD) isosurfaces can be loaded and rendered in our web application, and are shown for our model of P3HT at progressive degrees of (b) proper dihedral torsion and (c) improper dihedral torsion.

show that the barrier to torsion changes as improper angle increases. Similarly, by isolating the effects of both styles of torsion, we determine that improper torsion generally imposes a stronger energetic penalty compared to dihedral torsion. In particular, simulations of PNDI-T suggest that it is possible for adjacent monomers in a conjugated backbone to be highly twisted and still maintain conjugation. This finding suggests an explanation as to why some D–A polymers can maintain good charge transport properties while highly strained (e.g., in stretchable organic transistors).

Our findings indicate that the inclusion of a modified characterization of improper torsion helps better describe the energetics of conjugated polymers. Thus, consideration of the improper torsion within a conjugated system is recommended for highly accurate models of semiconducting polymers. Improper torsion is even more likely to be important when high degrees of torsion are present in general (e.g., films under strain, polymers deposited from melt, films annealed at high temperatures).

Further exploration of highly sterically hindered polymers (particularly D–A polymers with asymmetric monomers) can provide information about the disruption of electronic delocalization in conjugated polymers. Additional work in this area could offer significant insights into the high mobilities of modern D–A polymers, many of which are amorphous or take advantage of short-range aggregation. Thus, accurate understanding of how chemical structure affects the morphology of a polymer solid offers an avenue for improving predictions of its physical (e.g., electronic and mechanical) properties.

2.6 Acknowledgements

Chapter 2, in full, is a reprint of the material as it appears in *The Journal of Physical Chemistry B*, 2025. Ramji, Robert S.; Kleinschmidt, Andrew T.; Bhamidipati, Shruti; Zhang, Leon; Chen, Alexander X.; Pascal, Tod A.; Lipomi, Darren J., American Chemical Society, 2025. The dissertation author was the primary investigator and author of this paper.

Chapter 3

Modeling Framework for Crosslinking in Quantum Dot Films

Se Young Park, Seongjae Lee, Robert S. Ramji, Jeehye Yang, Hyeokjun Kim, Yoonsang Ham, Myoungjin Park, Tod A. Pascal, Darren J. Lipomi, and Moon Sung Kang. Additive-Type vs. Ligand-Type Crosslinkers for Direct Photopatterning of Robust Quantum Dot Network. *Manuscript under review*.

3.1 Introduction and Motivation

Direct photopatterning of colloidal quantum dots (QDs) through ligand photocrosslinking is a promising route to high-resolution emissive pixels for display applications.[48–51] The strategy translates the logic of a negative-tone photoresist to a thin QD film: a spin-coated film is selectively irradiated through a photomask, the exposed region forms an insoluble crosslinked network, and a developing solvent removes the unexposed region.[52,53] The appeal of crosslinking the organic ligand shell, rather than chemically transforming the inorganic core, is that QD luminescence can in principle be preserved.[54,55]

Crosslinking chemistry can be introduced in two distinct ways. In the additive-type approach, a bifunctional crosslinker is blended into the QD ink and interlocks the native ligands of neighboring QDs upon irradiation.[56,57] In the ligand-type approach, a photocrosslinkable moiety is anchored directly to the QD surface through a partial ligand exchange, so that one end of the crosslinker is already bound to a QD before exposure.[54,58] In the work described here, both crosslinker designs share an identical benzophenone (BP) photochemistry activated under

i-line UV irradiation (365 nm). The additive-type crosslinker, O-BP-2-LiXer, carries a BP group at each end of the molecule; the ligand-type crosslinker, O-BP-1-PXL, carries the same BP group at one end and a thiol anchor at the other. Upon irradiation the BP group abstracts a hydrogen atom from a nearby alkyl group, generating a ketyl radical that forms a covalent bond with an oleic acid (OA) ligand of an adjacent QD.[54]

The two designs differ sharply in their experimentally measured crosslinking efficiency. Efficiency was quantified through the film thickness retention ratio (FRR), the fraction of film thickness retained after immersion in the developing solvent (n-octane). When the number of crosslinkers per QD was matched at 44 molecules per QD, the ligand-type O-BP-1-PXL reached the threshold for sufficient crosslinking (FRR > 0.95) at a UV dose of only $1.1\,\mathrm{J\,cm^{-2}}$, whereas the additive-type O-BP-2-LiXer required $4.8\,\mathrm{J\,cm^{-2}}$ to reach the same threshold (Figure 3.1a). This lower dose requirement matters because UV exposure degrades QD photoluminescence: at its minimal effective dose the O-BP-1-PXL film retained a photoluminescence quantum yield (PL QY) of 109% relative to the pristine film, while the O-BP-2-LiXer film at its higher minimal dose fell to 67% (Figure 3.1b).

The central question addressed by the computational work in this chapter is mechanistic: why does the ligand-type crosslinker require so much less UV dose? Two explanations are plausible. The first is a connectivity argument: because one end of O-BP-1-PXL is pre-anchored to the QD surface, it needs to form only a single new bond to bridge two QDs, whereas the bifunctional O-BP-2-LiXer must form two bonds. The second is a geometric argument: the fixed orientation of the surface-anchored crosslinker might present its reactive group more favorably toward a neighboring QD. To distinguish between these explanations, and to connect single-crosslinker reactivity to the film-scale connectivity that governs FRR, I constructed an atomistic model of the crosslinked QD system, simulated the crosslinking reaction directly, and embedded the resulting local connectivity statistics into a percolation model of the macroscopic film.

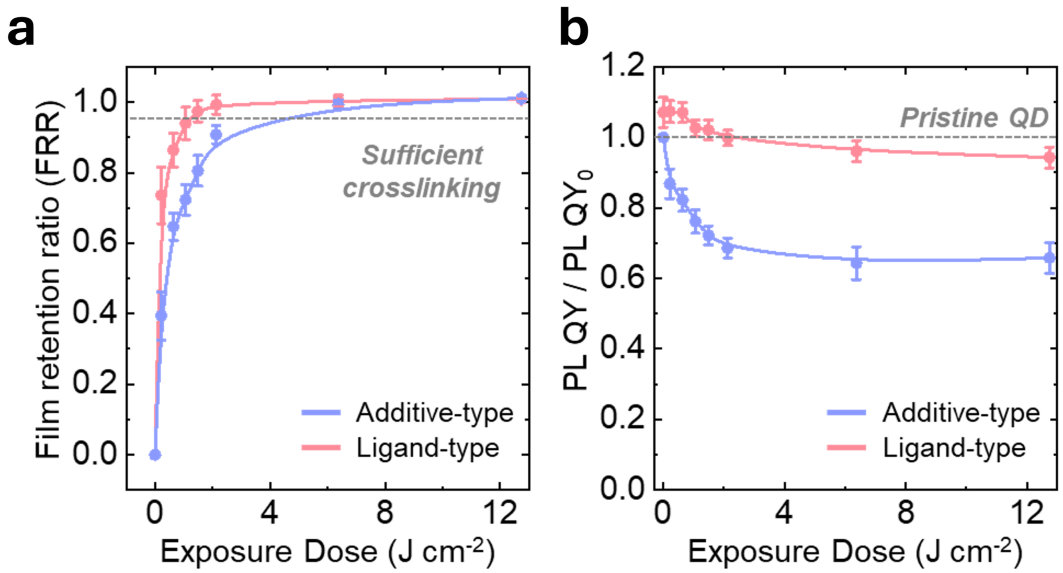

Figure 3.1. Experimental crosslinking efficiency that the simulations seek to explain. (a) Film thickness retention ratio (FRR) of crosslinked InP/ZnSeS QD films as a function of UV exposure dose for the additive-type (blue) and ligand-type (red) crosslinkers; the dashed line marks FRR = 0.95. (b) Normalized PL QY of the same films as a function of exposure dose; the dashed line marks the PL QY of the pristine film. Panels are reproduced from the corresponding figure of the source manuscript. The ligand-type crosslinker reaches sufficient crosslinking (FRR > 0.95) at $1.1\,\mathrm{J\,cm^{-2}}$, the additive-type at $4.8\,\mathrm{J\,cm^{-2}}$.

3.2 Construction of the Atomistic QD Model

Atomistic models of the QDs, ligands, crosslinkers, and their interfaces were built to match the materials used experimentally as closely as practical. The model InP/ZnSeS QD comprised an InP core of radius 1.2 nm and a ZnSeS shell of thickness 2.3 nm, giving a total radius of 3.5 nm (a 7 nm diameter particle), consistent with the experimental QDs. The InP core was generated by carving a sphere of radius 1.2 nm from a zincblende supercell. The shell was created as a random alloy of 44% ZnS and 56% ZnSe, matching the experimental shell composition, by carving a spherical shell from a bulk zincblende supercell; its lattice constant of 5.559 Å was obtained from Vegard's law. The core was placed inside the shell, and the assembled QD was minimized and equilibrated for 1 ns at 300 K in the NVT ensemble using a Nosé-Hoover thermostat with a Stillinger-Weber force field parameterized for II-VI materials.[59,60] The equilibrated inorganic particle was then treated as a rigid body in all subsequent crosslinking and stress-strain simulations.

Atomistic representations of OA and of the two crosslinkers, O-BP-1-PXL and O-BP-2-LiXer, were constructed in Avogadro[61,62] according to their chemical structures (Figure 3.2a). Optimized geometries and RESP partial charges for the deprotonated ligands and crosslinkers were computed at the ωB97X-D/6-311++G** level. Intermolecular interactions among the organic species were described with the DREIDING force field,[63] which is well suited to the aromatic and aliphatic moieties present in OA and the BP crosslinkers.

Describing the ligand-QD interface required additional care, because validated, transferable classical force-field parameters for the ZnS/ZnSe-ligand interface are not available in standard libraries.[64,65] I adopted a pragmatic effective model rather than a fully reactive or reparameterized interface potential. The Zn-rich shell was treated as passivated by anionic, oleate-like and thiolate-like ligands, a binding picture supported by density functional theory studies of anionic ligand passivation on cation-rich II-VI surfaces.[66–68] Inorganic partial charges were derived from composition-weighted, slab-derived Bader charge magnitudes ($q(\mathrm{Zn}) = +0.793$,

$q(\mathrm{S}) = -0.877$, $q(\mathrm{Se}) = -0.727$), reflecting the 44% S and 56% Se shell composition. These charges were obtained from Quantum ESPRESSO calculations on zincblende ZnS and ZnSe slabs[69,70] using the PBE functional with ultrasoft pseudopotentials from the SSSP library,[71–73] plane-wave cutoffs of 50 Ry (wavefunctions) and 400 Ry (charge density), and a $4 \times 4 \times 1$ Monkhorst-Pack k-point mesh, with all parameters selected by convergence testing.

Ligand-QD nonbonded interactions were otherwise described with UFF parameters. Because the generic UFF cross-terms underestimate the strong anchoring of carboxylate and thiolate groups to the Zn-rich surface, only the two nonbonded cross-interactions governing surface anchoring, Zn-O (carboxylate) and Zn-S (thiolate), were tuned empirically. Each was scaled by a factor of approximately 12. The scaling was guided by 1 ns MD simulations of the full particle in which the Zn-O and Zn-S radial distribution functions were monitored; scaling was halted once the radial distribution functions indicated saturated surface coverage, so as not to over-constrain the ligand shell. The resulting parameterization reproduces stable ligand adsorption and the qualitative trend of stronger thiolate than oleate binding. It should be understood as an effective model chosen to stabilize the bound-shell configuration, not as a unique description of the true interface potential.

Ligand and crosslinker counts were set from the experimental surface density of roughly 2 ligands nm^{-2} and the matched loading of 44 crosslinkers per QD. For a 7 nm QD this corresponds to 350 OA ligands and 44 additive-type crosslinkers for the LiXer QD, and 306 OA ligands plus 44 photocrosslinkable ligands (350 ligands in total) for the PXL QD. The PXL QD was built by randomly substituting 44 O-BP-1-PXL molecules for OA ligands on the QD surface, while the LiXer QD was built by adding 44 O-BP-2-LiXer molecules directly to the system. Each model QD was then replicated in the x direction to form a two-QD unit cell, which was the basic system for all subsequent crosslinking simulations (Figure 3.2b). Periodic boundary conditions made this two-QD cell representative of a bulk crosslinked film.

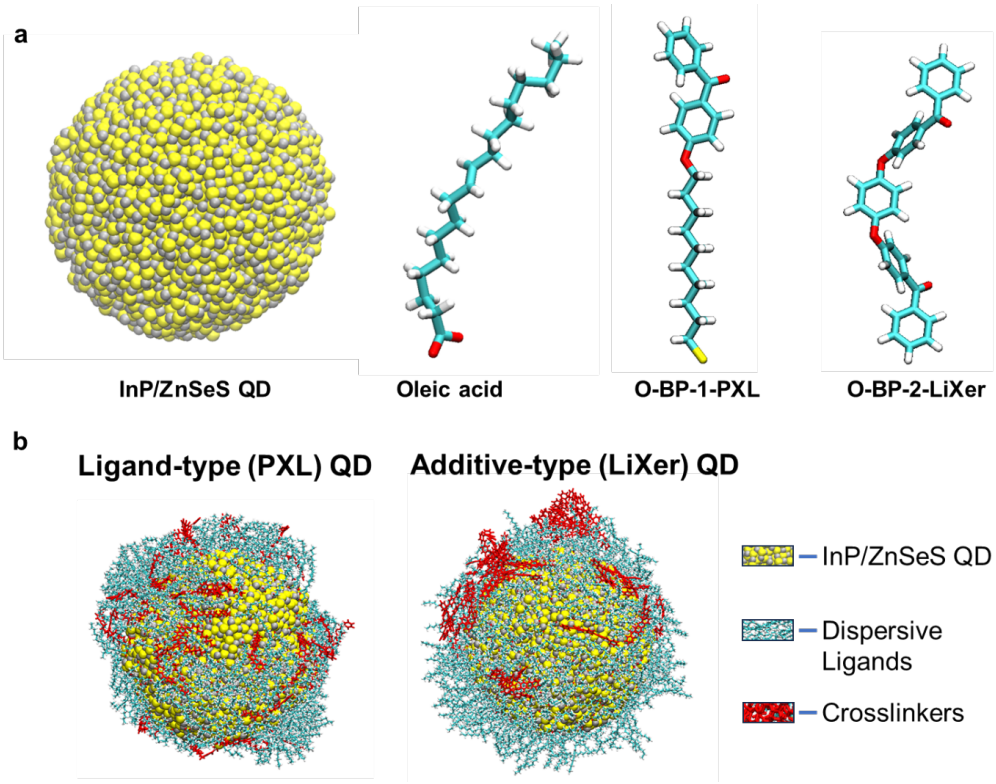

Figure 3.2. Atomistic models used in the crosslinking simulations. (a) Structures of the model InP/ZnSeS QD (core not shown for clarity), oleic acid, the ligand-type crosslinker O-BP-1-PXL, and the additive-type crosslinker O-BP-2-LiXer, from left to right. (b) Assembled ligand-type (PXL) and additive-type (LiXer) model QDs, showing the inorganic QD (yellow), the dispersive OA ligands (cyan), and the crosslinkers (red).

3.3 Crosslinking Simulations

Crosslinking was simulated directly on 50 independently randomized two-QD unit cells for each crosslinker type, so that a wide range of ligand conformations and crosslinking contacts would be sampled. To prepare each starting structure, one model QD was given a random rotation (without displacing its center of mass), the cell was replicated along x, heated to 500 K for 20 ps in the NVT ensemble, and then cooled to 300 K over 100 ps in the NPT ensemble at 1 atm. The cooled structure served as the starting point for the iterative crosslinking procedure.

All MD simulations were performed in LAMMPS.[74] The temperature was controlled by a Nosé-Hoover thermostat with a 100 fs relaxation time, and stresses were relaxed with an Andersen barostat (1 ps pressure relaxation). The equations of motion follow Shinoda and coworkers,[75] which combine the hydrostatic formulation of Martyna and coworkers[76] with the Parrinello-Rahman strain energy,[77] integrated with the time-reversible, measure-preserving Verlet integrators of Tuckerman et al.[78]

The crosslinking algorithm proceeded in cycles, summarized in Figure 3.3a. Each cycle consisted of (i) energy minimization, (ii) heating to 300 K for 20 ps in the NVT ensemble, and (iii) equilibration for 100 ps in the NPT ensemble at 1 atm to relax the ligand, crosslinker, and QD positions. After equilibration, the final frame was searched for crosslinking contacts, defined as a reactive BP oxygen within 4 Å of an alkyl carbon. When several candidate contacts were found, the closest was selected. A selected contact was converted into a permanent bond by forming a carbon-carbon bond between the alkyl carbon and the carbon adjacent to the BP oxygen, and transferring one of the alkyl carbon's hydrogen atoms to the BP oxygen to form a hydroxyl group, mimicking the experimental ketyl-radical hydrogen-abstraction mechanism. The cycle was repeated until either all crosslinkable groups had reacted or three consecutive cycles produced no new contacts.[79,80] The ParmEd[81] and MDAnalysis[82] libraries were used to process the trajectories and identify crosslinking contacts within the unit cell and its periodic images.

Each crosslink was classified by the connectivity it produced (Figure 3.3c). A bridging crosslink connects ligands on two different QDs and therefore contributes to the percolating network; an internal crosslink connects two ligands on the same QD and does not; an incomplete crosslink has reacted with one OA ligand but does not yet connect any QDs; and a non-activated crosslinker has not reacted at all. The incomplete category is available only to the bifunctional additive-type crosslinker: the ligand-type crosslinker begins each simulation already anchored to one QD, in an effectively incomplete state, so it can only form bridging or internal crosslinks. The key observable extracted from these simulations is the nearest-neighbor (NN) bond probability, the probability that two adjacent QDs are connected by at least one bridging crosslink, which is a direct measure of local connectivity in the film.

The simulations revealed a substantial efficiency difference between the two crosslinker types. Both approached 100% NN bond probability as the reaction neared completion, but the two diverged sharply at low extents of reaction (Figure 3.3b). Below 40% reaction, the ligand-type crosslinker (PXL) produced an NN bond probability up to 2.9 times greater than the additive-type crosslinker (LiXer). The distribution of bond types makes the mechanism explicit (Figure 3.3d): at a given extent of reaction the additive-type system accumulates a large population of incomplete crosslinks, because a bifunctional crosslinker must react twice before it can bridge or close internally, whereas the ligand-type system converts reacted groups into bridging or internal crosslinks immediately. Importantly, beyond 50% crosslinking the additive-type crosslinker forms slightly more bridging crosslinks than the ligand-type, which confirms that the ligand-type advantage at low reaction extents is not a geometric effect of crosslinker orientation on the QD surface. The advantage arises from the single-bond requirement for completing a ligand-type crosslink.

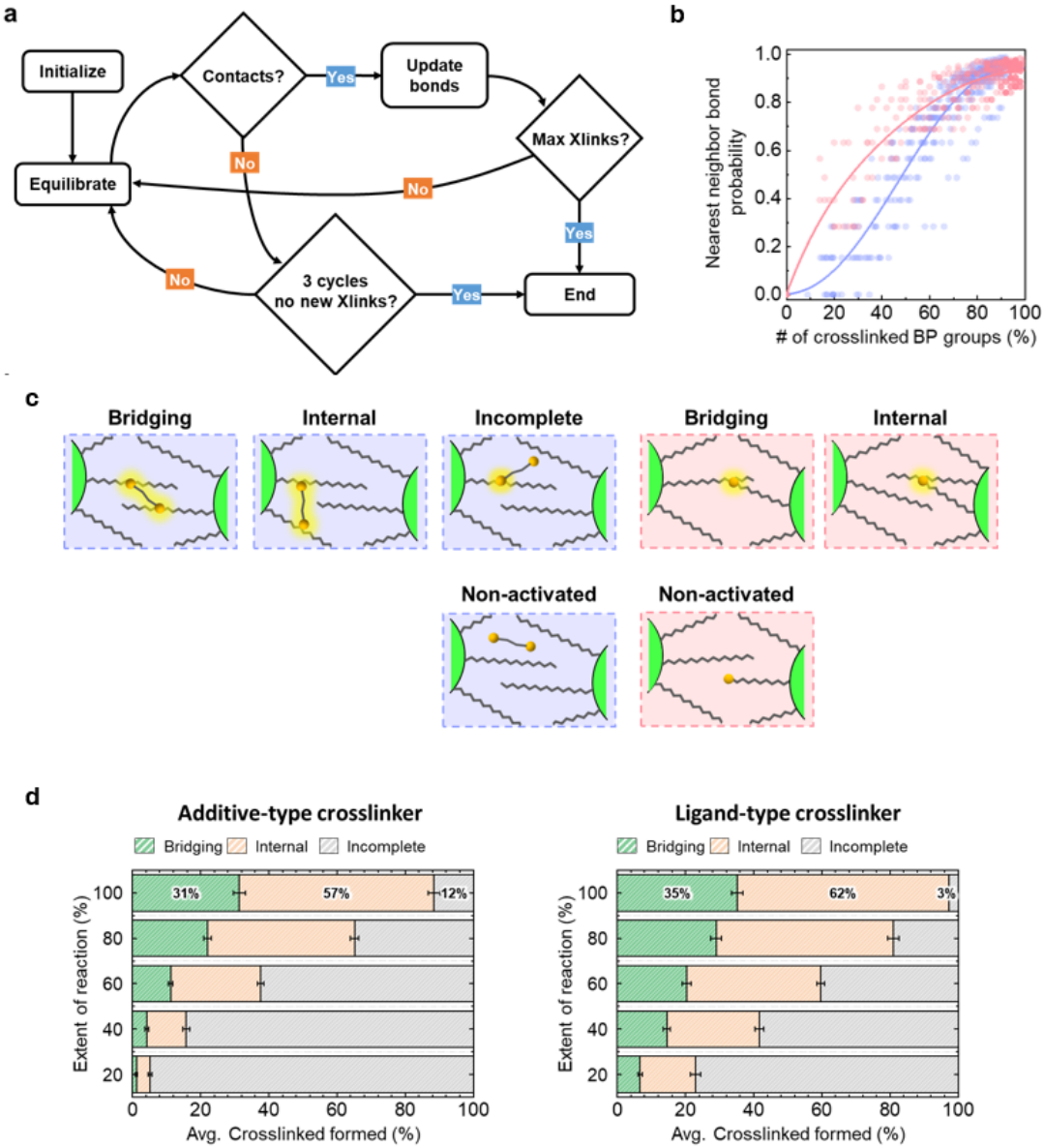

Figure 3.3. Crosslinking simulations of the two-QD model. (a) Iterative crosslinking protocol: equilibrate, search for contacts, update bonds, and terminate when the maximum number of crosslinks is reached or three cycles yield no new contacts. (b) Nearest-neighbor bond probability as a function of the percentage of crosslinked BP groups for the additive-type (blue) and ligand-type (red) crosslinkers; the dashed line marks the bond probability required for 95% connectivity from the percolation analysis (Section 3.4). (c) Classification of crosslink outcomes for the additive-type (left) and ligand-type (right) systems: bridging, internal, incomplete, and non-activated. The incomplete state is accessible only to the bifunctional additive-type crosslinker. (d) Average populations of crosslink types through the progression of the reaction; the ligand-type crosslinker reaches critical connectivity at a much lower extent of reaction than the additive-type crosslinker.

3.4 Percolation Analysis and Connection to Film Retention

The crosslinking simulations report local connectivity between adjacent QDs, but FRR is a film-scale property: a film resists dissolution only when its QDs form a spanning network. To translate local NN bond probability into film-scale connectivity, I implemented a Monte Carlo bond-percolation model on a three-dimensional hexagonal close-packed (hcp) lattice, in which each lattice node represents a QD and each potential nearest-neighbor bond is present with probability p equal to the NN bond probability from the MD simulations.

The Monte Carlo approach was first validated against the literature. On a $10 \times 10 \times 10$ hcp lattice the model reproduced the established critical bond probability for percolation onset, $P_c \approx 0.12$, in close agreement with published values for the hcp lattice.[83] (Figure 3.4b). With the method validated, I used it to determine the threshold needed for film integrity rather than merely for percolation onset. Modeling the film as a $50 \times 50 \times 3$ lattice and sampling each value of p 100 times, the model showed that an NN bond probability of approximately 0.298 is required to connect 95% of the nodes to the spanning network (Figure 3.4c, and Figure 3.5). This 95% connectivity threshold, P_{95}, was chosen to approximate the experimental requirement of FRR > 0.95 for an acceptable, development-stable film. The same P_{95} value was obtained on a bulk $10 \times 10 \times 10$ lattice, indicating that the threshold is relatively insensitive to film thickness over this range.

Combining the percolation threshold with the crosslinking simulations closes the argument. Because UV dose controls the extent of BP reaction, the NN bond probability can be expressed as a function of the fraction of crosslinked BP groups, and the percolation threshold then fixes the extent of reaction required to reach film-scale connectivity. The threshold-crossing analysis (Figure 3.4d) shows that the additive-type system must crosslink more than three times as many BP groups as the ligand-type system to reach equivalent 95% connectivity. This factor of three in required reaction extent is the simulated counterpart of the roughly four-fold difference in experimental UV dose (4.8 versus 1.1 $\mathrm{J\,cm^{-2}}$). The remaining discrepancy is consistent with

the nonlinear relationship between UV dose and BP conversion and with the conservative nature of the connectivity threshold, and it does not affect the qualitative conclusion.

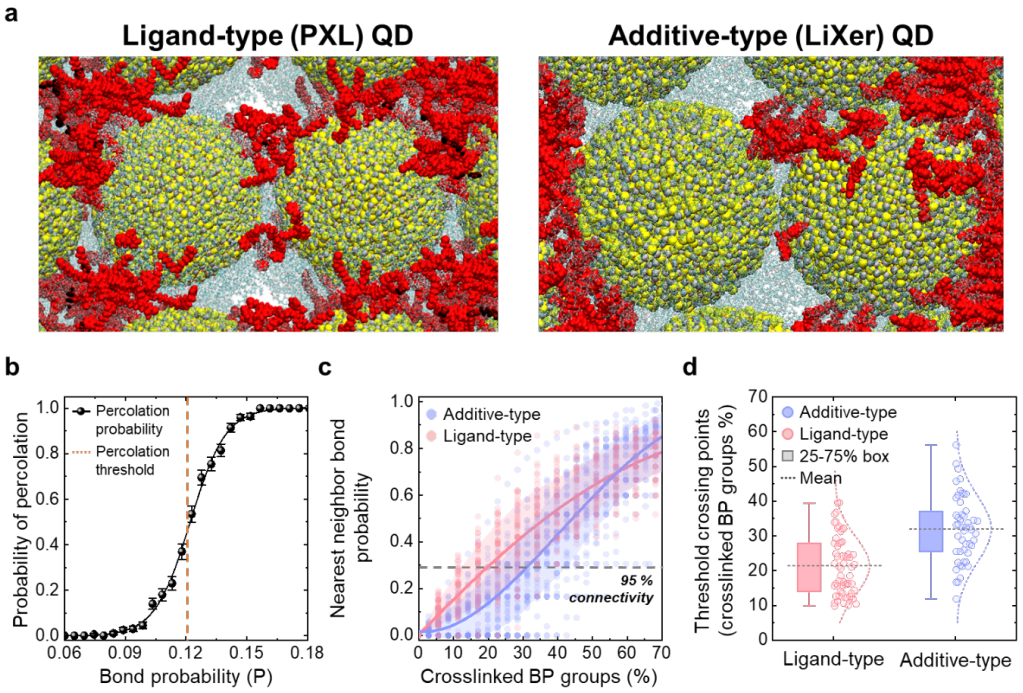

Figure 3.4. Percolation analysis linking local connectivity to film-scale integrity. (a) Representative snapshots of crosslinked ligand-type (PXL) and additive-type (LiXer) films, showing the QDs (yellow), dispersive ligands (cyan), and crosslinkers (red). (b) Monte Carlo percolation on a $10 \times 10 \times 10$ hcp lattice, reproducing the literature percolation threshold near 0.12. (c) Nearest-neighbor bond probability as a function of the percentage of crosslinked BP groups for both crosslinker types, with the 95% connectivity threshold marked. (d) Threshold-crossing points, the percentage of crosslinked BP groups at which each system reaches the 0.298 nearest-neighbor bond probability required for 95% connectivity; the additive-type system requires substantially more reacted BP groups.

3.5 Summary

The molecular simulations developed in this chapter explain, at the mechanistic level, why a ligand-type benzophenone crosslinker patterns QD films at a far lower UV dose than a chemically identical additive-type crosslinker. By building an effective atomistic model of the InP/ZnSeS QD and its ligand shell, simulating the crosslinking reaction directly across 50 randomized configurations per crosslinker type, and embedding the resulting local connectivity

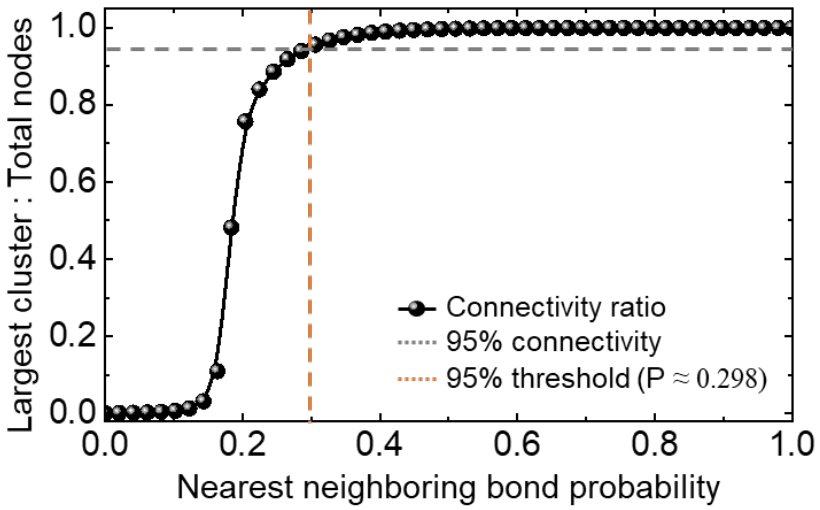

Figure 3.5. Determination of the 95% connectivity threshold. Monte Carlo bond-percolation result for a film modeled as a $50 \times 50 \times 3$ hcp lattice, plotted as the ratio of the largest connected cluster to the total number of nodes against nearest-neighbor bond probability. The 95% connectivity level (gray dashed line) is reached at a nearest-neighbor bond probability of approximately 0.298 (orange dashed line), which is adopted as the threshold P_{95} corresponding to the experimental FRR > 0.95 criterion.

statistics in a validated percolation model, I showed that the ligand-type advantage stems from a connectivity argument rather than a geometric one. A surface-anchored crosslinker needs to form only one new bond to bridge two QDs, so it converts reacted BP groups into network-forming crosslinks immediately, whereas a bifunctional additive-type crosslinker accumulates incomplete crosslinks until enough of its groups have reacted. Quantitatively, the additive-type system must crosslink more than three times as many BP groups to reach the same 95% film connectivity, mirroring the experimental dose gap. The framework also illustrates a transferable strategy: single-junction reactivity sampled by direct MD crosslinking can be coupled to lattice percolation to predict a macroscopic, processing-relevant property, the film thickness retention ratio, from molecular-scale chemistry.

3.6 Acknowledgements

Chapter 3, in part, has been submitted for publication of the material. Park, Se Young; Lee, Seongjae; Ramji, Robert S.; Yang, Jeehye; Kim, Hyeokjun; Ham, Yoonsang; Park, Myoungjin; Pascal, Tod A.; Lipomi, Darren J.; Kang, Moon Sung. The dissertation author was the primary investigator and author of the computational portions of this material.

Chapter 4

Thermodynamics and Molecular Mechanism of Reversible, Peptide-Induced Aggregation in Colloidal Gold Nanoparticles

Robert Ramji, Margaret Mullooly, Isla Duncan, William Brown, Benjamin Lam, Darren J. Lipomi, Kristina D. Closser, Jesse V. Jokerst, and Tod A. Pascal. Thermodynamics and Molecular Mechanism of Reversible, Peptide-Induced Aggregation in Colloidal Gold Nanoparticles. *Manuscript in preparation*.

4.1 Abstract

Aggregation-based colorimetric assays exploit the distance-dependent plasmonic coupling of gold nanoparticles (AuNPs) and are widely used for sensitive detection. Because aggregation is normally irreversible, such assays are single-use and tolerate only narrow ranges of pH and ionic strength. Short cationic peptides induce a reversible form of aggregation with a potency that depends on sequence rather than on net charge alone, but the thermodynamic driving forces behind it are uncharacterized. We present an atomistic molecular dynamics framework that measures the free energy of bringing two citrate-capped AuNPs together, with explicit citrate, counterions, and 25 peptide copies, and that resolves every structural observable against the same coordinate on which the free energy is measured. Across twelve peptides plus controls, the compression free energy over 47 to 27 Å is repulsive for the anionic peptide ($+8.4$ kcal mol^{-1}) and for the bare citrate shell ($+7.7$), progressively screened by NaCl ($+3.7$, $+2.3$, $+0.8$ at 0.1, 0.2, and 0.5 M) but never inverted by monovalent salt, flat for neutral Gly_2 ($+1.5$), and attractive

for every cationic peptide (-10.6 to -27.0). Net charge sets this repulsive to attractive axis, and the structural record shows how: cationic peptides displace Na^+ from the gap before contact and then bridge the two anionic surfaces, while the citrate shell remains a spectator and the metal cores contribute nothing above 27 Å. Charge is not the whole law: at identical $+1$ charge His_2 is attractive (-12.6) where Gly_2 is flat, and at $+3$ Arg_2 is more attractive than Lys_2 (-27.0 against -15.8). The free-energy barrier moves outward with peptide charge in step with the onset of bridging, identifying the barrier top as the point at which bridging switches on. Equilibrium umbrella sampling reproduces the approach branch independently, agreeing on barrier position to within 1.1 Å and on barrier height to within 0.8 kcal mol^{-1}. The model recovers the class distinctions available from experiment: stability without peptide, screening by salt that never inverts, attraction for every cationic sequence, and inactivity for neutral Gly_2.

4.2 Introduction

Gold nanoparticles (AuNPs) have emerged as versatile platforms in biomedical diagnostics and therapeutic delivery, owing to their tunable plasmonic properties, high surface-area-to-volume ratio, and well-established surface chemistry.[84–86] A particularly compelling property of AuNP dispersions is their strong distance-dependent optical response: upon aggregation, the plasmon resonance of neighboring particles couples, producing a characteristic red-to-blue colorimetric shift visible to the naked eye.[87] This phenomenon has been exploited extensively in colorimetric assays for the detection of nucleic acids, proteins, small molecules, heavy metals, and pathogens.[88–91] In most aggregation-based assay designs, however, the assembly process is irreversible, because the van der Waals attraction between metal cores at short interparticle separation is large compared with thermal energy. Once aggregated, the particles cannot be returned to their dispersed state, which constrains such sensors to single-use formats. The aggregation step is also highly sensitive to the chemical environment, limiting the range of media in which a given sensor can operate.

Experimental work has demonstrated that citrate-capped AuNPs can be induced to aggregate reversibly when the assembly is mediated by cationic peptides, with the dispersed state recoverable upon removal or dilution of the peptide, or upon competitive exchange with thiolated ligands.[92,93] This behavior is mechanistically distinct from conventional salt- or antibody-induced irreversible aggregation. The reversal is attributed primarily to a reduction in interparticle electrostatic repulsion rather than to direct metal contact, so that dispersive thiol-bearing ligands can subsequently displace the peptide and citrate and re-stabilize the particles.[94,95] The precise sequence of molecular events that governs assembly, the thermodynamic driving forces involved, and the structural basis of reversibility have nonetheless not been characterized at the atomic level.

AuNPs and their interactions with both citrate and peptides have received considerable computational attention. Molecular dynamics and density functional theory studies have established that citrate binds Au surfaces in a coverage- and pH-dependent manner, with the protonation state of the carboxylate groups strongly influencing surface affinity and layer structure.[96–98] Force-field parametrizations for the Au and citrate interface have been developed and compared against ab initio predictions and against spectroscopic characterization of citrate structuring on Au,[99–101] providing a foundation for atomistic models of citrate-capped AuNPs in explicit solvent; complementary work has examined implicit-solvent treatments of the same systems.[97,102] Broader studies of AuNP aggregation have used DLVO-based continuum models and, more recently, coarse-grained molecular dynamics to describe the kinetics and thermodynamics of assembly. These approaches, however, sacrifice the molecular detail at the peptide and citrate interface that is likely essential for understanding sequence-dependent aggregation.[103–105] Direct atomistic studies of AuNP and peptide association remain comparatively sparse, leaving a mechanistic gap that experimental measurements alone cannot close.

A prior computational effort began to address this gap by computing binding free-energy profiles for a small set of citrate-capped AuNP and peptide systems.[106] That study provided a first atomistic view of these systems and recovered the experimental contrast between the cationic

RRK peptide, which induces reversible aggregation, and control systems with no peptide or with a nominally neutral peptide (GG). We note that the peptides follow our collaborators' synthetic convention of C-terminal amidation, so that even a nominally neutral sequence such as GG carries a net charge of $+1$ at neutral pH. No prior study, however, has examined peptide-mediated AuNP aggregation systematically across a sequence series, which is required to connect molecular structure to measured aggregation thresholds.

Two mechanistic pictures compete for peptide-induced aggregation of anionic citrate-AuNPs. In the first, purely electrostatic picture, cationic peptides adsorb, neutralize the citrate shell's charge, collapse the double-layer repulsion, and, with two or more cationic groups, crosslink neighboring particles; aggregation potency should then track net charge and be reproducible with any cation. In the second, chemistry-specific picture, particular side chains engage the gold surface or the citrate shell in ways that a generic ammonium group does not, so that potency depends on sequence and on where the special residue sits within it. Experiment alone cannot separate these two pictures, because the measured peptide panel is only five sequences deep and the strong and weak aggregators differ in more than one respect at once. What can adjudicate between them is a molecular model that contains the citrate shell, the counterions, and many peptide copies explicitly, that measures a free energy of aggregation along a defined coordinate, and that records what rearranges along that coordinate so that structure and thermodynamics can be compared frame for frame.

Here we develop and apply such a framework. We simulate the approach of two citrate-capped AuNPs across a twelve-peptide series designed to separate net charge from side-chain chemistry, spanning net charges from -1 to $+3$ and including three pairs of sequences that differ only in residue order. Free energies of compression are obtained from bidirectional steered molecular dynamics (SMD) work and cross-validated against equilibrium umbrella sampling with MBAR. Structural observables resolved along the same coordinate identify the molecular events responsible. We then set the resulting free energies beside the experimental behavior of the same system at the level the comparison supports, and use the structural record to identify

the molecular event that ends the repulsive regime.

4.3 Methods

4.3.1 Experimental Aggregation Potencies

Citrate-capped AuNPs of approximately 20 nm diameter were prepared by the Turkevich method as reported previously.[95] Sodium citrate tribasic dihydrate (150 mg in 5 mL of deionized water) was added to boiling $HAuCl_4 \cdot 3H_2O$ (45 mg in 300 mL of deionized water) at 120 °C under vigorous stirring and allowed to react for 15 min. The solution was cooled to room temperature, centrifuged to remove unreacted reagents, and the particles redispersed in deionized water.

Peptides were synthesized by automated solid-phase synthesis on an Aapptec Eclipse synthesizer using Rink-Amide MBHA resin, cleaved, precipitated in cold diethyl ether, and purified by reverse-phase HPLC with the signal monitored at 220 nm; identity was confirmed by ESI-MS and MALDI-TOF MS.[95] Every sequence therefore carries a free NH_2 N-terminus and a $CONH_2$ C-terminus, which is the terminal chemistry assumed when assigning peptide net charges in the simulations (Section 4.3.5).

Aggregation was quantified by UV-vis spectroscopy. AuNPs (100 μL) were added to peptide (10 μL) at varying concentration in a 96-well plate and spectra were recorded after 15 min on a BioTek Synergy H1 plate reader. Assembly intensity is the ratio of the absorbance at the aggregated peak wavelength to the absorbance at 520 nm, so that the ratio is high when the particles are clustered and low when they are dispersed. Assembly intensities were fitted to a sigmoidal dose-response curve in GraphPad Prism 10, and C_{50} was defined as the concentration at which assembly intensity reaches half its maximal value; a lower C_{50} therefore indicates a more potent aggregator. Measurements were made at pH 7 in deionized water with no added buffer or supporting electrolyte, which is the condition the simulations approximate, since the simulated cells contain only the counterions required for neutrality.

Potencies are available for five of the twelve simulated sequences: HK 0.141, HR 0.139, RR 0.338, KH 0.977, and RH 0.954 μM. Gly_2 was measured and produced no appreciable absorbance shift at concentrations up to 100 μM, so its C_{50} is undefined and it serves as an inactive control rather than as a weak aggregator. Asp_2 and Gly_4 were not measured, and no experimental claim is made for them. The RR value is consistent with the 0.34 μM reported for the same peptide and particle preparation.[95] Each C_{50} is the fitted midpoint of a dose-response curve measured in triplicate. These values establish that the cationic dipeptides aggregate at micromolar concentration; the comparison drawn in Section 4.10 is at the level of active against inactive rather than between individual sequences.

4.3.2 Molecular Dynamics Simulations

All molecular dynamics simulations were performed with the LAMMPS atomistic simulation engine[34] using a 1 fs timestep. Simulations were conducted in implicit solvent with a uniform dielectric constant of 78 to approximate aqueous conditions, and long-range electrostatics were treated with the particle-particle particle-mesh (PPPM) solver[35,107] at a relative accuracy of 10^{-5}. Van der Waals and short-range electrostatic interactions used the lj/charmm/coul/long pair style[108] with a 13 Å inner and 14 Å outer cutoff. Lorentz-Berthelot mixing rules were applied to all van der Waals interactions not otherwise specified, and the van der Waals and Coulomb contributions of 1-4 interactions were scaled by 0.5 and 5/6 respectively, following AMBER convention. Bonds involving hydrogen were constrained with the SHAKE algorithm.[109] Temperature was maintained at 300 K with a Nosé-Hoover thermostat[110,111] using a 100 fs relaxation time. The integration scheme follows the time-reversible, measure-preserving Verlet integrators of Tuckerman and co-workers.[36] The simulation cell measured $200 \times 100 \times 100$ Å.

4.3.3 Nanoparticle Model

Gold nanoparticles of approximately 2.1 nm diameter (236 Au atoms) were constructed by carving a sphere from a bulk face-centered-cubic gold supercell. Lennard-Jones parameters for gold were taken from Heinz and co-workers,[112] which provide accurate representations of FCC metal surfaces using a 12-6 Lennard-Jones potential. Gold atoms carry no partial charge.

4.3.4 Force-Field Parameterization

Citrate and peptide structures were built in Avogadro.[113] Geometries were optimized and atomic partial charges derived with the RESP method[114] at the B3LYP/6-311++G** level under implicit solvent using the SS(V)PE solvation model[115] with a dielectric constant of 78.39, as implemented in Q-Chem 4.[29] Bonded and nonbonded parameters for citrate and all peptides were assigned with the General AMBER Force Field (GAFF)[24] via Antechamber.[116] GAFF was chosen over the CHARMM-based parameterizations that dominate the citrate-gold literature because it provides consistent coverage of the full set of dipeptides and of citrate within a single parameterization, and because the peptide partial charges are derived here from first principles rather than transferred; the tradeoff is that the citrate-gold interface is described by generic mixing rather than by parameters fitted to that interface, which we return to in Section 4.11.3. Lennard-Jones parameters for Na^+ and Cl^- were taken from Jensen and Jorgensen.[117] A scaling factor of 1/10 was applied to the Lennard-Jones ε parameter for Na^+ and Au interactions to prevent ions from adhering to the gold surface, an artifact of the large diagonal ε term for Au combined with the simplified implicit-solvent treatment.

4.3.5 System Construction and Equilibration

Each nanoparticle was assembled and equilibrated individually. Twenty-five trisodium citrate molecules were placed around the AuNP to achieve a surface density of approximately 2 molecules nm^{-2}, consistent with experimentally measured citrate coverage, and charge-balancing Na^+ counterions were added. To seed citrate adsorption, a temporary harmonic steering force

drew citrate molecules within the Lennard-Jones cutoff of the Au surface; after approximately 1 ns the steering force was removed and the system was equilibrated in the NVT ensemble at 300 K for 10 ns.

The equilibrated single-NP structure was replicated along the x dimension to generate a symmetric two-nanoparticle cell. For peptide-containing systems, 25 peptide molecules were added together with the number of Cl^- counterions required to neutralize the cell; all peptides were C-terminally amidated with a free N-terminus, to reflect experimental conditions. Net charges per peptide copy, computed from the assigned partial charges, were DD -1; GG, GGGG, and HH $+1$; HK, KH, HR, and RH $+2$; and KK, KR, RK, and RR $+3$. Histidine was modeled in its neutral form throughout, appropriate to pH 7. Peptide-containing systems carry their own counterions but no additional buffer salt, so the Cl^- content scales with peptide charge (25, 50, and 75 Cl^- for the $+1$, $+2$, and $+3$ series against 150 Na^+ in every case). Citrate-only controls were run salt-free and at 0.1, 0.2, and 0.5 M added NaCl. A bare two-particle system with no citrate, peptide, or ions was also constructed. The assembly sequence is illustrated in Figure 4.1.

All systems were then equilibrated for 5 ns under NVT at 300 K to distribute peptides and counterions. Equilibration runs followed a common protocol: conjugate-gradient energy minimization, gradual heating from 0 to 300 K over 50 ps under NVT, and NVT dynamics. These runs establish the configuration from which biased sampling begins and are not interpreted thermodynamically; their role is to confirm that the starting state is a properly coated particle pair rather than a random dispersion of ligands. At the end of equilibration approximately 97% of peptide chains are adsorbed to a gold surface.

4.3.6 Steered Molecular Dynamics

Production simulations used steered molecular dynamics implemented through the PLUMED 2 plugin[118] interfaced with LAMMPS. A moving harmonic restraint with spring constant $\kappa = 5$ kcal mol^{-1} Å^{-2} was applied to the center-of-mass (COM) distance between the two nanoparticles, defined by their respective Au atom groups. After an initial compression from

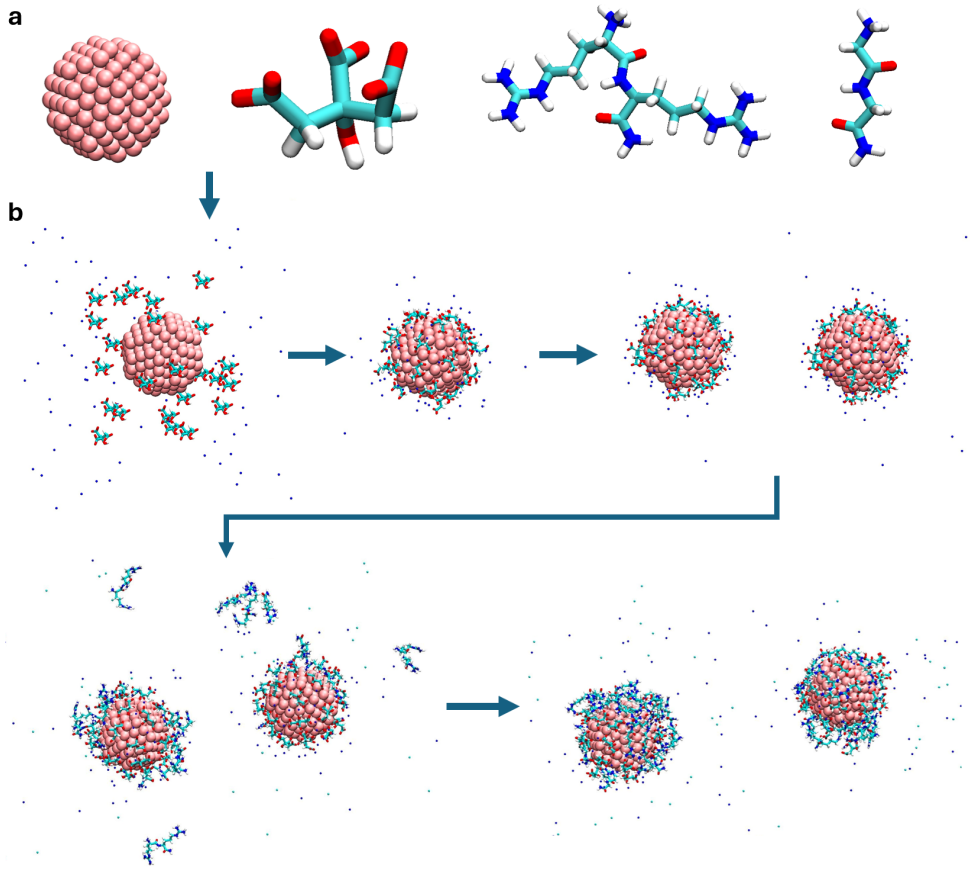

Figure 4.1. Atomistic model components and assembly process. (a) Primary components of the model: a 2.1 nm diameter AuNP, citrate^{3-}, amidated diarginine^{3+}, and amidated diglycine^{1+}. (b) Assembly sequence: random placement of citrate^{3-} and Na^{+} around the bare AuNP, brief thermalization, cell replication along x, random placement of peptides and Cl^{-}, and a final thermalization to distribute peptides and counterions.

approximately 100 Å, each system was subjected to 30 half-cycles alternating between 50 and 25 Å at 1 ns per leg, for 30 ns of production (Figure 4.2). Coordinates were written every 5,000 steps and the instantaneous COM distance and applied force were recorded by PLUMED every 100 steps to a COLVAR file. A slower variant at 4 ns per leg was run for RR as a pull-rate check. For the bare-core system the restraint was stiffened to $\kappa = 20$ and $\kappa = 100$ kcal mol^{-1} Å^{-2}, because at lower stiffness the bare cores overcame the restraint and fused irreversibly.

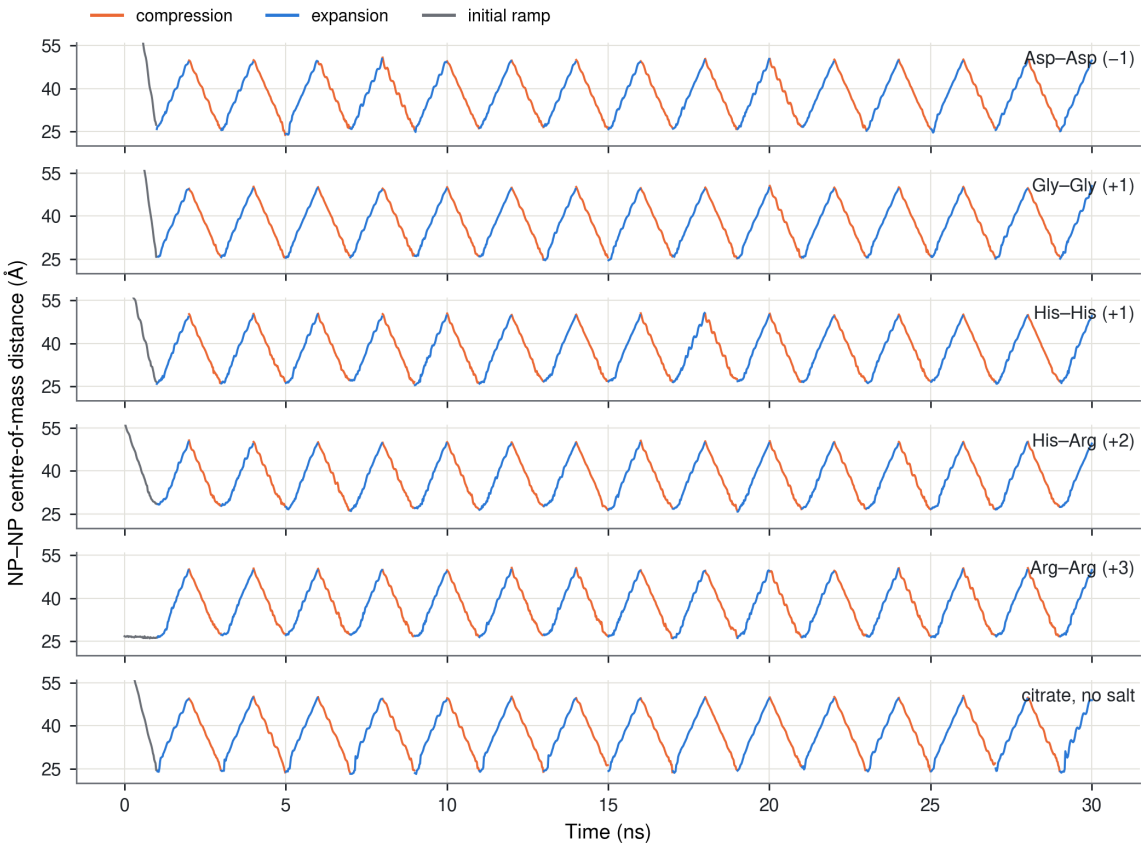

Figure 4.2. Steered molecular dynamics protocol. Interparticle center-of-mass distance against time for six representative systems, with the initial ramp from wide separation in gray and the alternating compression and expansion half-cycles in color. Each system was driven through 30 half-cycles at 1 ns per leg between 50 and 25 Å; the work over the 27 to 47 Å window common to every complete half-cycle is what enters the free-energy estimators of Section 4.3.7.

4.3.7 Free-Energy Estimators

Each half-cycle records the work done by the moving restraint. Over the window 27 to 47 Å, which every complete half-cycle spans, the reversible and dissipated parts of the work are separated as

$$\Delta G = \frac{\langle W_{\mathrm{push}} \rangle - \langle W_{\mathrm{pull}} \rangle}{2}, \qquad W_{\mathrm{diss}} = \frac{\langle W_{\mathrm{push}} \rangle + \langle W_{\mathrm{pull}} \rangle}{2}, \tag{4.1}$$

where the averages run over the fifteen legs in each direction. This is the symmetric, Gaussian-work limit of the Crooks fluctuation theorem[1] and of the Bennett acceptance ratio,[2] and it involves no exponential averaging.

This estimator was adopted in preference to a one-directional Jarzynski average[119] because at 25 Å ns^{-1} the pulls are far from quasi-static: dissipation is comparable to $|\Delta G|$ for the strongly binding sequences, and an exponential average over fifteen legs with tens of kcal mol^{-1} of spread in the work is dominated by the single lowest-work trajectory. Applied to these runs, the one-directional estimator returns positive, and therefore unphysical, binding free energies. The push-pull asymmetry, by contrast, carries the sign robustly even when dissipation is large. Two checks support this. First, the asymmetry is diagnostic in cases where the compression work alone is not: His_2 compresses as easily as Gly_2 ($W_{\mathrm{push}} \approx 5$ kcal mol^{-1} for both) but resists expansion far more ($W_{\mathrm{pull}} \approx 30$ against 2), which is attraction and not friction. Second, the $4\times$ slower RR pull reproduces the value obtained at the production rate (-28.5 against -27.0 kcal mol^{-1}), so the estimate is not a pull-rate artifact.

The same decomposition applied to the instantaneous restraint force, rather than to the integrated work, yields a continuous profile: averaging the mean force measured on the compression and expansion branches at each value of the coordinate cancels the leading frictional contribution, and integrating the result inward from 47 Å gives a free-energy curve rather than a pair of endpoints. Across the twelve-peptide panel the endpoint of this curve agrees with the work-based ΔG to within 1.9 kcal mol^{-1} on average and 3.1 kcal mol^{-1} at worst, well inside the dissipation scale. All profiles and barrier landmarks reported below are obtained this way; no

quantity in this work derives from an exponential work average.

Reported uncertainties on ΔG are standard errors over the legs of a single trajectory. Because consecutive half-cycles of one run are not independent, these should be read as lower bounds on the true uncertainty.

4.3.8 Umbrella Sampling

Equilibrium free energies were computed independently by umbrella sampling[3] using 61 windows spaced 0.5 Å apart from 20 to 50 Å in the COM distance, with a harmonic PLUMED restraint of $\kappa = 5$ kcal mol^{-1} Å^{-2} in each window. Sets were run for citrate (40 ns per window), RR (10 and 40 ns), GG (10 ns), HK (10 ns), and KH (10 ns). All windows were seeded from a single configuration near 26 Å. Free energies were reconstructed with MBAR[5] including statistical-inefficiency decorrelation, per-window sampling diagnostics, and a connectivity guard that restricts the estimate to windows forming a chain of adequate overlap; WHAM[4] was used as a cross-check.

4.3.9 Trajectory Analysis

Trajectory analysis used the MDAnalysis package[120,121] through a purpose-built analysis package that caches per-frame and per-molecule observables once and resolves each against the interparticle coordinate, with compression and expansion branches kept separate. Because LAMMPS data files carry no residue naming, all per-molecule analyses use fragment-based selection together with explicit atom-index ranges defined in the input files. Observables comprise radial distribution functions between selected atom groups, radius of gyration of citrate and peptide molecules, adsorbed-citrate coverage and denticity, surface charge at the Stern plane, Na^+ and Cl^- populations in the interparticle gap, and molecular bridging. A molecule is counted as bridging when it lies within 6 Å of both gold surfaces simultaneously. Each observable was gated on its Spearman association with the interparticle gap so that responders and spectators could be separated on a common criterion.

4.4 Results: Unbiased Simulations

To illustrate the model's behavior under equilibrium conditions, we performed unbiased 20 ns NVT simulations of four systems: bare AuNPs, citrate-capped AuNPs with counterions, citrate-capped AuNPs with GG, and citrate-capped AuNPs with RR (Figure 4.3). The bare system collapsed into an irreversibly fused state. The citrate-capped systems with no peptide and with GG both remained dispersed throughout. The RR system aggregated during the run and remained aggregated for its remainder. Unlike the fusion seen for bare particles, the aggregated RR particles stayed separated by their citrate and peptide coating layers and never reached direct metal contact.

This contact-separated geometry is the structural signature expected for reversible, peptide-induced assembly: the particles are bound but held above the irreversible primary minimum of the DLVO interaction, preserving a coating layer that thiol-bearing dispersants can later displace to redisperse the particles. It is the clearest visual statement of the distinction between the peptide-mediated and the bare-particle outcome, and it motivates the free-energy analysis that follows.

These runs are single trajectories, one per system, and we treat them as illustrative rather than as evidence. Four systems cannot validate a twelve-peptide series, and with one trajectory each no statement about relative rates or probabilities is available. Everything quantitative in this work comes from the biased sampling described below.

4.5 Results: What Rearranges on Approach

Because the structural cache and the restraint work come from the same trajectories, every observable can be read against the coordinate on which the free energy is measured (Figure 4.4). Gating each observable on its Spearman association with the interparticle gap separates responders from spectators cleanly and consistently across all fourteen SMD systems. Peptide bridging is the strongest responder, with ρ ranging from -0.61 for DD and GG to

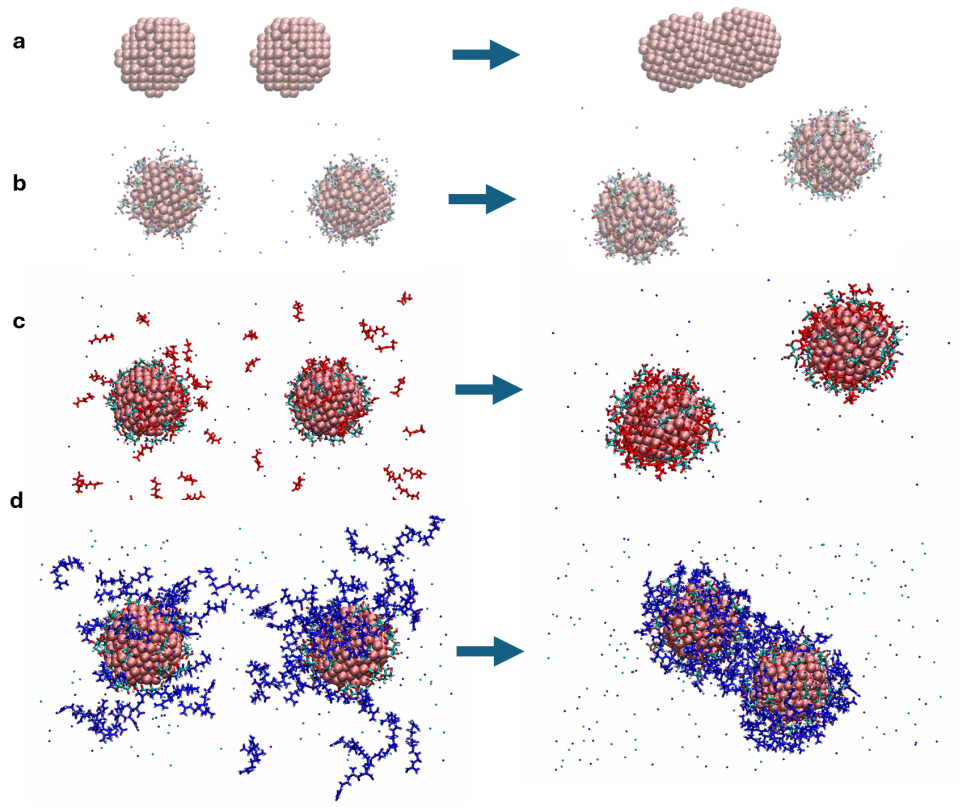

Figure 4.3. Unbiased 20 ns NVT simulations, shown at the start (left) and end (right) of each run. (a) Bare AuNPs fuse into a single particle. (b) Citrate-capped AuNPs with counterions remain dispersed. (c) Diglycine (GG) added to citrate-capped AuNPs does not induce aggregation. (d) Diarginine (RR) induces aggregation, but the particles remain separated by intact peptide and citrate layers rather than reaching metal contact. One trajectory per system.

-0.85 for KR, becoming more negative for more cationic peptides. Citrate bridging follows at -0.55 to -0.71, turning on only below about 8 Å of surface gap. The Na^+ population in the gap responds positively, from $+0.10$ for the citrate control and DD to $+0.54$ for KR, meaning counterions leave the gap on compression and do so most for the cationic peptides (Figure 4.5). Surface charge at the Stern plane regulates only weakly, -0.09 to -0.30. Citrate coverage, citrate denticity, and peptide radius of gyration all give $|\rho| < 0.1$: the citrate shell is neither squeezed out nor rebound as the particles approach. It is a spectator, in agreement with earlier simulations of this system reporting that the citrate ligand is not displaced during aggregation.[106]

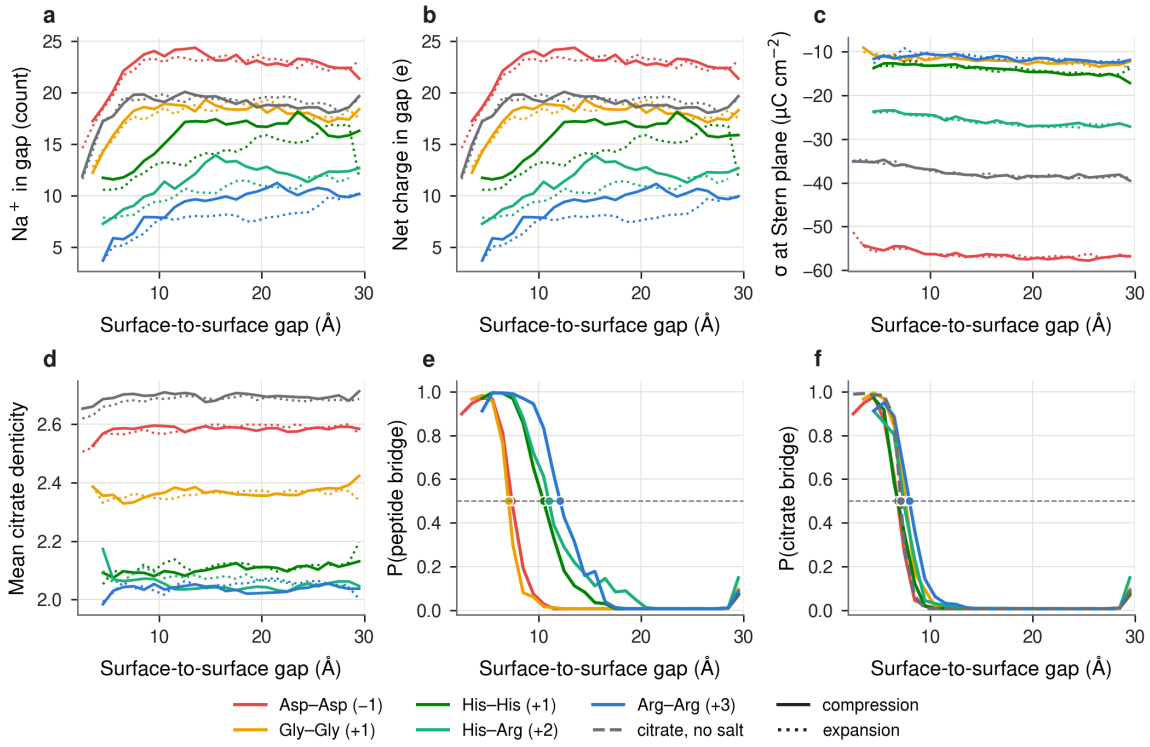

Figure 4.4. Structural observables resolved against the surface-to-surface gap for the ladder Asp_2, citrate, Gly_2, His_2, His-Arg, and Arg_2, with compression (solid) and expansion (dotted) branches shown separately. (a) Na^+ population in the interparticle gap. (b) Net charge in the gap. (c) Surface charge density at the Stern plane. (d) Mean citrate denticity. (e) Probability that a peptide bridges both surfaces, with 50% onsets marked. (f) Probability that a citrate bridges both surfaces. Bridging occurs in every system near contact, including the anionic and neutral controls, while citrate denticity and Stern-plane charge barely respond.

4.6 Results: Free Energy Across the Peptide Series

Table 4.1. Compression free energy over 47 to 27 Å from bidirectional SMD work, in kcal mol^{-1}. Dissipation is the symmetric part of the same work decomposition and sets the scale on which magnitudes should be read.

System	Net charge	ΔG	Dissipation	Class
Asp_2 (DD)	-1	$+8.4$	5.0	anionic
bare Au cores	0	-0.5 / -0.7	0.1 / 0.0	$\kappa = 20$ / 100
citrate, no salt	0	$+7.7$	1.1	control
citrate, 0.1 M NaCl	0	$+3.7$	1.2	control
citrate, 0.2 M NaCl	0	$+2.3$	1.2	control
citrate, 0.5 M NaCl	0	$+0.8$	1.6	control
Gly_2 (GG)	$+1$	$+1.5$	3.2	neutral
Gly_4 (GGGG)	$+1$	-7.8	6.6	neutral, longer
His_2 (HH)	$+1$	-12.6	17.3	His
Lys-His (KH)	$+2$	-10.6	16.9	His, C-terminal
His-Lys (HK)	$+2$	-13.7	16.5	His, N-terminal
Arg-His (RH)	$+2$	-18.0	22.9	His, C-terminal
His-Arg (HR)	$+2$	-18.3	23.1	His, N-terminal
Lys_2 (KK)	$+3$	-15.8	20.9	cationic
Arg-Lys (RK)	$+3$	-22.7	30.2	cationic
Lys-Arg (KR)	$+3$	-24.8	30.5	cationic
Arg_2 (RR)	$+3$	-27.0	27.6	cationic
Arg_2, 4 ns per leg	$+3$	-28.5	23.4	slow-pull check

Four comparisons isolate the effects at work (Table 4.1). A like-charged peptide adds nothing: Asp_2 at $+8.4$ sits with bare citrate at $+7.7$, so the double-layer repulsion is intact. Bridge geometry alone is not the driver: neutral Gly_2 bridges both surfaces below 7 Å yet its ΔG is flat at $+1.5$. Monovalent screening is real but bounded: the salt series is monotonic at $+7.7$, $+3.7$, $+2.3$, and $+0.8$ kcal mol^{-1} for 0, 0.1, 0.2, and 0.5 M NaCl, approaching zero without inverting. Salt removes the barrier; it does not supply an attraction. And the metal cores contribute nothing over the comparison window: two citrate-free Au cores give ΔG(47 to 27 Å) of -0.5 and -0.7 kcal mol^{-1} at $\kappa = 20$ and 100 with dissipation near zero, the two stiffnesses agreeing. Core-core attraction switches on only below about 27 Å, that is at a surface gap under 6 Å: -2.9 and -3.0 at 25 Å, -4.9 and -5.7 at 24 Å, and -11.4 at 23 Å. Everything in Table 4.1

over 27 to 47 Å is therefore an adsorbate and electrolyte effect, with the cores mattering only at contact.

Every cationic peptide is attractive, from -10.6 for KH to -27.0 for RR, so net charge sets the coarse repulsive to attractive axis. But the extended panel shows this is not a complete law. At fixed $+1$, His_2 is strongly attractive at -12.6 where Gly_2 is flat, and Gly_4 is intermediate at -7.8: neutral histidine and chain length add attraction that charge does not predict, enough that His_2 rivals some $+2$ peptides. At fixed $+3$, arginine outperforms lysine, with Arg_2 at -27.0 against Lys_2 at -15.8 and the mixed pairs in between at -22.7 and -24.8; guanidinium engages the citrate carboxylates more strongly than ammonium does. At fixed $+2$, the arginine-containing pairs at about -18 are more attractive than the lysine-containing ones at -10.6 to -13.7. Within each pair, N-terminal histidine is more attractive than C-terminal (HK -13.7 against KH -10.6; HR -18.3 against RH -18.0), but these differences are smaller than the dissipation scale and we do not rest any claim on their magnitudes.

The honest synthesis is that the interaction is charge-dominated and chemistry-modulated. Charge decides whether the approach is repulsive or attractive; side-chain identity, chain length, and the arginine against lysine distinction tune the magnitude, in the case of His_2 by enough that charge alone mispredicts.

4.7 Results: The Barrier Coincides with the Onset of Bridging

The mean-force reconstruction described in Section 4.3.7 gives a continuous free-energy profile for every system, and with it the position and height of the repulsive maximum on the approach. Both quantities order with charge (Figure 4.6). The barrier moves outward and shrinks monotonically along the series, from 27.0 Å and $+7.8$ kcal mol^{-1} for DD, through 30.9 Å and $+5.5$ for GG, 34.6 Å and $+2.9$ for GGGG, 36.0 to 37.1 Å and $+1.9$ to $+2.3$ for His_2 and the lysine-histidine pairs, to 41.0 to 42.2 Å and $+0.3$ to $+0.8$ for the $+3$ peptides. A residual

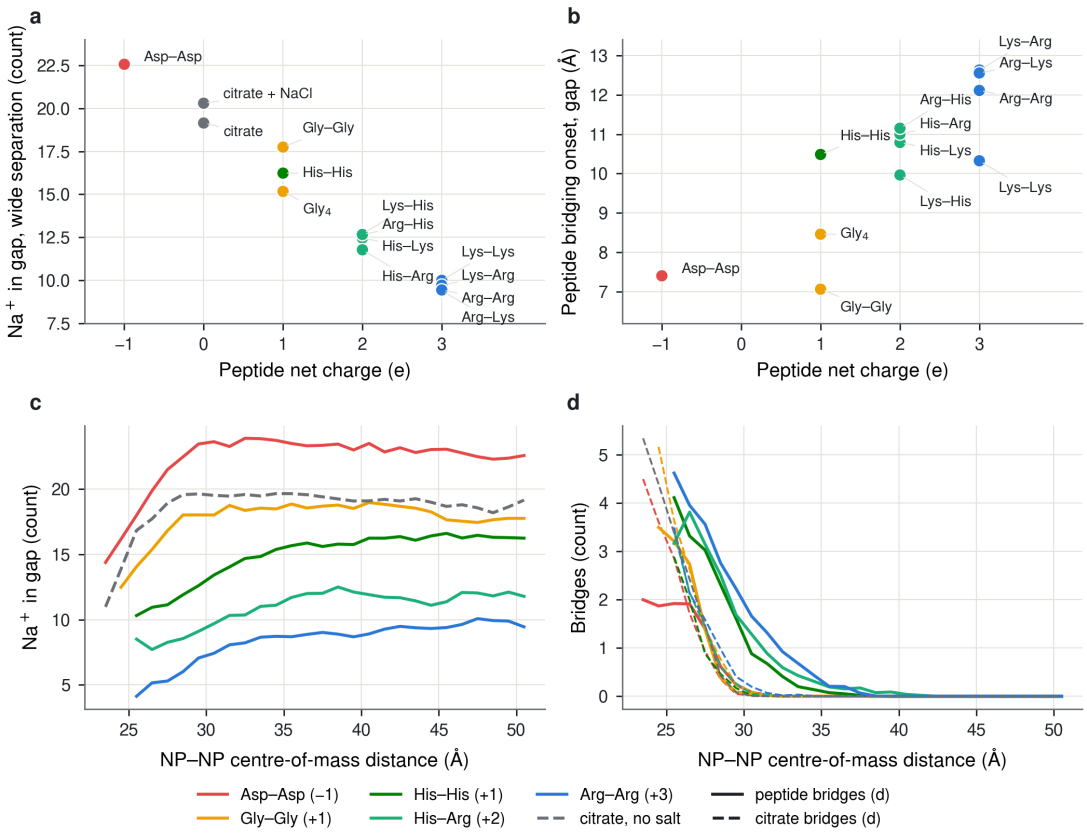

Figure 4.5. Structural quantities against peptide net charge and against interparticle separation. (a) Na^+ population in the gap at wide separation, before the particles interact. (b) Peptide bridging onset, expressed as a surface gap. (c) Na^+ population against center-of-mass distance. (d) Peptide and citrate bridge counts against center-of-mass distance. Counterion depletion and bridging both order with net charge before the particles are in contact.

short-range repulsion therefore persists even for the strongest binders until bridges engage.

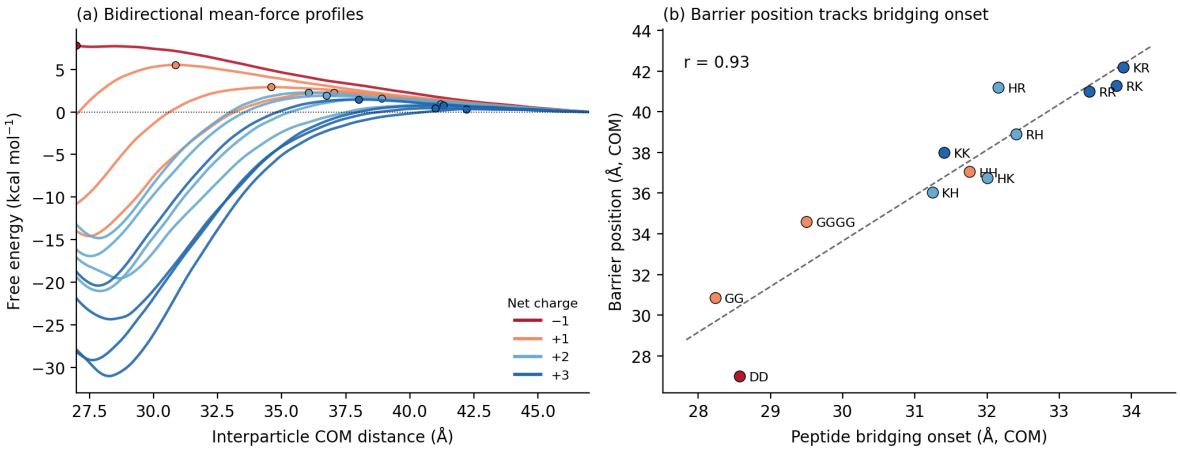

Figure 4.6. (a) Bidirectional mean-force free-energy profiles for the twelve peptides, referenced to 47 Å and colored by net charge, with the position of the repulsive maximum marked on each curve. (b) Barrier position against the 50% onset of peptide bridging, expressed on the same center-of-mass coordinate; the dashed line is a least-squares fit. Asp_2 lies below the trend because its maximum is pinned at the inner edge of the 27 Å analysis window, so its barrier position is a lower bound.

Placing the two quantities side by side shows that they are not independent. Across the twelve peptides the barrier position tracks the 50% onset of peptide bridging with a Pearson correlation of 0.93 and a Spearman correlation of 0.94, and the barrier maximum sits consistently a few ångström outside the separation at which bridging begins. The free energy turns over just as the first bridges form. The one system that departs from the trend is DD, whose maximum falls at the inner edge of the analysis window and is therefore a lower bound rather than a located maximum.

This is the point at which the structural and thermodynamic descriptions meet. The preceding sections established separately that cationic peptides lower the barrier and that they bridge the two surfaces earlier; the correlation says these are the same event observed in two ways. It also refines the mechanism: bridging is not merely correlated with aggregation, it is what ends the repulsive regime. Since bridging occurs in every system near contact, including the repulsive ones, what distinguishes the cationic peptides is not that they bridge but that they bridge

far enough out to intercept the approach before the double-layer repulsion has fully developed.

4.8 Results: Salt Screening and Dose Response

The citrate-only salt series isolates pure electrostatic screening from any peptide-specific effect. Compression free energy falls monotonically from $+7.7$ kcal mol^{-1} salt-free to $+3.7$, $+2.3$, and $+0.8$ at 0.1, 0.2, and 0.5 M NaCl, with the Debye length of the added salt contracting from 9.6 to 6.8 to 4.3 Å (Figure 4.7). The 150 citrate counterions contribute a further 0.06 M or so to the ionic strength of every system. The series approaches zero without crossing it: monovalent salt removes the barrier but never supplies an attraction. Whatever the cationic peptides do, it is not simply screening.

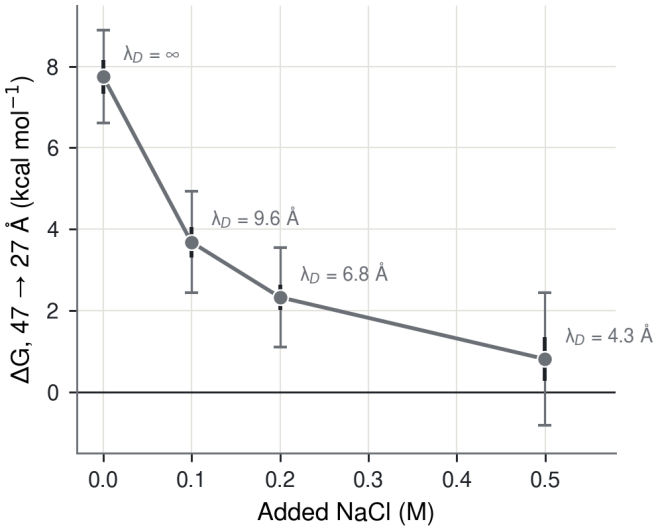

Figure 4.7. Compression free energy of the citrate-only control against added NaCl concentration. Screening is monotonic and approaches zero without inverting.

Running the same protocol with 5, 10, 15, 20, and 25 Arg_2 chains gives a simulated dose response (Figure 4.8). Over the full window the free energy is close to linear in chain count, at -2.3, -6.5, -12.9, -20.6, and -27.0 kcal mol^{-1}, an increment of roughly -1.2 kcal mol^{-1} per chain with no sign of saturation up to 25 chains. The long-range branch from 47 to 30 Å is more informative: with 10 chains or fewer the outer double-layer repulsion survives at $+3.9$

and $+2.8$ kcal mol^{-1}, down from the citrate control's $+7.4$, and attraction is confined to contact. Between 10 and 15 chains, corresponding to 30 to 45 cationic charges against 150 citrate charges, the approach branch itself turns attractive, reaching -2.3, -16.5, and -18.7 kcal mol^{-1} at 15, 20, and 25 chains.

The transferable quantity here is the peptide-to-citrate charge ratio rather than a concentration: 25 chains in this cell is roughly 21 mM, which is not comparable with a micromolar C_{50}, and each step of the series also changes the Cl^- content. The threshold ratio of 0.2 to 0.3 is the meaningful number, and it is the quantity to set beside an experimental titration against peptide-to-particle ratio if one is available.

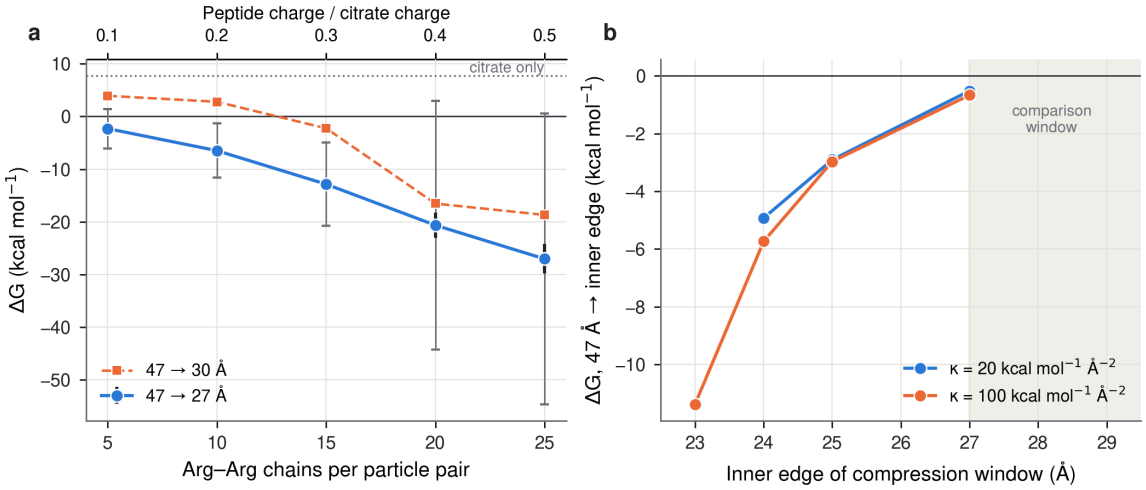

Figure 4.8. (a) Arg_2 chain-count series: compression free energy against number of chains per particle pair, for the full window (47 to 27 Å) and for the long-range branch (47 to 30 Å), with the peptide-to-citrate charge ratio on the upper axis and the citrate-only value marked. (b) Bare-core baseline against the inner edge of the integration window at two restraint stiffnesses, showing that core-core attraction begins only below about 27 Å.

4.9 Results: Equilibrium Umbrella Sampling

Steered dynamics and umbrella sampling share only the force field and the reaction coordinate. Agreement between them is therefore a genuine robustness check rather than a consistency check, and we ran umbrella sets for five systems to obtain it.

Windows inside roughly 28 to 30 Å drift from their restraint centers and do not reach adequate overlap with their neighbors, so no estimator can produce a trustworthy profile across that region. All estimates below are therefore restricted to the connected chain of outer windows, and the depth of the bound well is not reported.

On that connected chain, MBAR yields approach-branch profiles with proper uncertainties, referenced to 45 to 50 Å (Figure 4.9). Citrate gives monotonic repulsion reaching $+5.5 \pm 0.1$ kcal mol^{-1} at 31.7 Å. Gly_2 gives a barrier of $+5.6$ at 30.7 Å falling to $+0.4 \pm 0.3$ at 27.7 Å. Arg_2 gives a barrier of $+1.3$ at 39.9 Å followed by steep attraction from about 38 Å inward. The two $+2$ histidine sets give the same shape as one another: a barrier of $+2.2$ kcal mol^{-1} at 36.6 Å for His-Lys and $+2.4$ at 35.5 Å for Lys-His, further in and higher than the Arg_2 barrier as expected for $+2$ against $+3$, followed by attraction reaching -12.9 ± 0.2 and -11.5 ± 0.3 kcal mol^{-1} respectively at 30 Å.

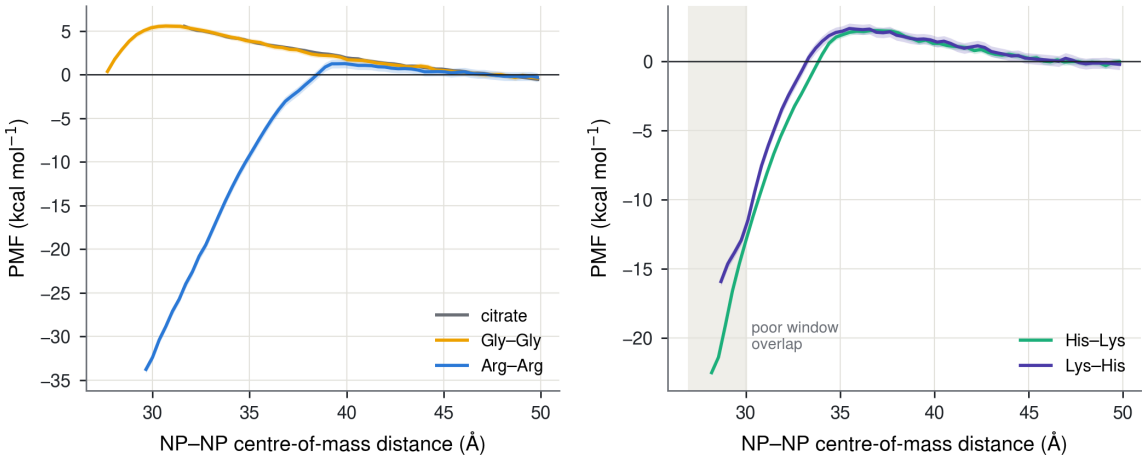

Figure 4.9. Equilibrium approach-branch potentials of mean force from MBAR, referenced to 45 to 50 Å. Left: citrate, Gly_2, and Arg_2. Right: the charge-matched pair His-Lys and Lys-His, with the region of poor window overlap shaded. Estimates are restricted to the connected chain of outer windows.

These equilibrium estimates agree with the bidirectional SMD work in sign and, on the approach branch, in magnitude to within a few kcal mol^{-1}: citrate gives $+7.4$ by SMD over 47 to 30 Å against $+5.5$ by umbrella at 31.7 Å, and Gly_2 gives $+1.5$ against $+0.4$ at 27.7 Å through

a barrier of 5.6 kcal mol^{-1} that the SMD profile also shows.

The comparison is sharper for the barrier, because the mean-force reconstruction of Section 4.7 provides a curve rather than endpoints. The two methods place the repulsive maximum at $+5.5$ against $+5.6$ kcal mol^{-1} and 30.9 against 30.7 Å for Gly_2; $+2.3$ against $+2.4$ and 36.0 against 35.5 Å for Lys-His; $+1.9$ against $+2.2$ and 36.8 against 36.6 Å for His-Lys; and $+0.5$ against $+1.3$ and 41.0 against 39.9 Å for Arg_2. Barrier positions agree to within 1.1 Å and heights to within 0.8 kcal mol^{-1} across four systems spanning the full range of behavior, which is a stronger statement than endpoint agreement alone.

Because the two estimators share no machinery beyond the force field and the coordinate, this agreement is the principal evidence that the free energies reported in Section 4.6 are not artifacts of the nonequilibrium protocol.

4.10 Comparison with Experiment

The simulated system differs from the measured one in particle size (2.1 against roughly 20 nm), in peptide concentration (25 chains per particle pair, of order 21 mM, against micromolar), and in peptide-to-particle stoichiometry. No quantitative comparison is therefore appropriate, and we make none. What the measurements do provide is a set of qualitative class distinctions, and the model reproduces all of them.

Citrate-capped AuNPs are colloidally stable in the absence of peptide, and the salt-free citrate control is the second most repulsive system in the panel at $+7.7$ kcal mol^{-1}, with a barrier of comparable size. Monovalent salt destabilizes them experimentally, and the simulated citrate repulsion falls monotonically with added NaCl to $+3.7$, $+2.3$, and $+0.8$ kcal mol^{-1} at 0.1, 0.2, and 0.5 M, approaching zero without inverting; salt removes the barrier rather than supplying an attraction, which is consistent with salt-induced aggregation being irreversible while peptide-induced aggregation is not.

Cationic dipeptides aggregate citrate-AuNPs at micromolar concentration, and every

cationic peptide in the panel is attractive, from -10.6 to -27.0 kcal mol^{-1}, with barriers at or below 2.3 kcal mol^{-1}. Gly_2 produces no measurable absorbance shift at concentrations up to 100 μM, and it is the only peptide whose simulated compression free energy is flat, at $+1.5$ kcal mol^{-1} behind a barrier of 5.5 kcal mol^{-1} that no cationic sequence retains. The anionic Asp_2, which was not measured, is more repulsive still.

The agreement is therefore three-way and directional: repulsive without peptide, screened but not inverted by salt, and attractive with cationic peptide, with a neutral sequence that fails to aggregate in both the experiment and the model. This is the level at which the present calculations can be tested, and at that level they hold across the full panel. Resolving differences between individual cationic sequences would require replica trajectories, slower pulls, and a simulated system matched to the experimental particle size and stoichiometry, none of which is attempted here.

4.11 Discussion

4.11.1 What the Present Data Settle

The sign of the interparticle interaction on the approach branch is set primarily by peptide net charge: anionic and neutral-glycine systems and the citrate baselines repel, and cationic peptides attract. Salt screens this repulsion without inverting it. Two independent estimators agree, and a fourfold slower pull reproduces the result.

The structural mechanism in the attractive cases is counterion release from the interparticle region followed by peptide bridging of the two anionic surfaces. The citrate shell is a spectator: its coverage, denticity, and Stern-plane charge do not respond to the approach. The metal cores are inert above 27 Å.

The barrier position coincides with the onset of bridging across the whole series, which identifies bridging as the event that ends the repulsive regime rather than merely as a correlate of aggregation.

Side-chain chemistry is a real second lever and not noise. His_2 at $+1$ is attractive where Gly_2 at $+1$ is flat; Arg_2 exceeds Lys_2 at $+3$; and chain length adds attraction independent of charge.

4.11.2 What They Do Not Settle

For any attractive case the sign of the free energy is clear but its origin is not. Direct side-chain to citrate enthalpy, in the form of arginine and lysine salt bridges or histidine hydrogen bonding and aromatic contacts, and the entropy of releasing displaced counterions from the confined gap to bulk, produce the same ΔG. The panel already contains the contrasts that would separate them, notably arginine against lysine at fixed $+3$ and His_2 against Gly_2 at fixed $+1$, but only a temperature-resolved enthalpy and entropy decomposition can do so. We make no enthalpic or entropic attribution here.

The depth of the bound well is likewise unresolved. The umbrella sets recover the approach branch reliably but not the region below roughly 28 Å, for the seeding reason diagnosed in Section 4.9, and the SMD magnitudes in that region carry a dissipation comparable to the free energy itself.

One methodological caution applies to any future temperature series. In an implicit solvent the Coulomb term is a solvent-averaged free energy whose entire temperature dependence resides in the dielectric constant. Holding ε fixed at 78 while scanning temperature would return zero solvation entropy and make an entropy-driven association appear enthalpic, which is a sign error rather than an uncertainty. Any van 't Hoff analysis of this system must use a temperature-dependent ε.

4.11.3 Limitations

One SMD trajectory per system was run, and the reported standard errors, computed over the legs of a single trajectory, understate the true uncertainty because consecutive half-cycles are correlated. Independent replicas with different seeds and starting configurations are the

single most important addition to this work, and are required before any difference smaller than the dissipation scale can be treated quantitatively, which includes every comparison between individual cationic sequences.

Pulling at 25 Å ns^{-1} leaves dissipation comparable to $|\Delta G|$ for the strong binders. Signs and large orderings are robust; magnitudes are soft.

An ionic-strength confound remains: peptide systems carry their own counterions but no added salt, so the $+3$ systems contain 75 Cl^- where the $+1$ systems contain 25. A salt-matched peptide series would remove it.

The simulated particles are 2.1 nm in diameter against roughly 20 nm experimentally, so curvature, facet distribution, and peptide-to-particle stoichiometry all differ from the measured system, which is why the comparison in Section 4.10 is restricted to qualitative class distinctions. The companion size study found that potency depends on particle size in a way that is not captured by van der Waals scaling alone,[122] so the size gap is a real limitation and not merely a matter of rescaling.

The implicit-solvent, fixed-charge model cannot represent hydration structure, polarization, image charges, or coordination of side chains to gold, all of which are plausible contributors to sequence-specific behavior that the present calculations cannot resolve. Related to this, GAFF is a minority choice for the citrate-gold interface, where CHARMM-based parameterizations predominate; the citrate shell behaves as a spectator throughout, which limits the exposure of the present conclusions to that choice, but an explicit-solvent calculation with an interface-fitted force field would be the appropriate validation.

Histidine is modeled in its neutral form throughout, appropriate to pH 7. A protonated-histidine set has been generated and would support a pH comparison, but it is not analyzed here and no claim about protonation-state dependence is made.

4.11.4 Next Steps

Several analyses are available from data already in hand: the solvent-reorganization contribution from the existing 300 K energy logs against separation, a citrate run at 1.0 M NaCl from an input deck already built, a salt-matched reanalysis, and a chain-count series for a histidine peptide. Beyond these, replica SMD pulls for the six most-used systems are inexpensive and would convert several of the orderings above from directional to quantitative, and slower pulls would shrink the dissipation across the panel. Extending the umbrella sets inward, by equilibrating each window from its already-equilibrated neighbor rather than from a common starting configuration, would resolve the bound well and is a prerequisite for any temperature series. Finally, an explicit-solvent calculation for one system on the approach branch would calibrate the implicit-solvent magnitudes.

A complementary coarse-grained model is under development to extend these mechanistic findings to the length and time scales at which aggregation is measured experimentally. The atomistic results reported here define what such a model must reproduce: the charge-dominated ordering, the counterion-release and bridging mechanism, the coincidence of the barrier with bridging onset, and the threshold charge ratio at which the long-range branch turns attractive.

4.12 Conclusion

We have presented an atomistic simulation framework for the aggregation of citrate-capped gold nanoparticles mediated by short cationic peptides, and applied it across a twelve-peptide series designed to separate net charge from side-chain chemistry. Bidirectional steered molecular dynamics gives compression free energies that are repulsive for the anionic peptide and the citrate baselines, screened but never inverted by monovalent salt, and attractive for every cationic peptide, with equilibrium umbrella sampling independently reproducing the approach branch in both barrier height and barrier position. Structural observables resolved along the same coordinate identify the mechanism as counterion release followed by peptide bridging,

with the citrate shell a spectator and the metal cores inert until contact. The repulsive barrier moves outward with peptide charge in step with the onset of bridging, which identifies bridging as the event that ends the repulsive regime rather than as a correlate of it.

Set beside experiment, the model reproduces the class distinctions that are available to test: colloidal stability without peptide, screening by monovalent salt that never inverts, attraction for every cationic sequence, and inactivity for neutral Gly_2. Discriminating among individual cationic sequences lies beyond what one trajectory per system at this pull rate can support, and we do not attempt it.

The central result is that one number, the position of the repulsive maximum, tracks a structural event, the onset of peptide bridging, across twelve sequences spanning four net charges and three residue-order pairs. Aggregation in this system is not a matter of peptides neutralizing a surface and letting van der Waals attraction take over: the metal cores contribute nothing until contact, and the citrate shell never reorganizes. What ends the repulsion is the first peptide reaching across the gap, and cationic peptides aggregate because they can reach across it sooner. That statement is testable, it follows from the free energies and the structural record together rather than from either alone, and it is what a coarse-grained or continuum description of this system would need to reproduce.

4.13 Acknowledgements

Chapter 4, in part, is currently being prepared for submission for publication of the material. Ramji, Robert; Mullooly, Margaret; Duncan, Isla; Brown, William; Lam, Benjamin; Lipomi, Darren J.; Closser, Kristina D.; Jokerst, Jesse V.; Pascal, Tod A. The dissertation author was the primary investigator and author of this material.

Bibliography

[1] Crooks, G. E. Entropy Production Fluctuation Theorem and the Nonequilibrium Work Relation for Free Energy Differences. *Phys. Rev. E* **1999**, *60*, 2721–2726.

[2] Bennett, C. H. Efficient Estimation of Free Energy Differences from Monte Carlo Data. *J. Comput. Phys.* **1976**, *22*, 245–268.

[3] Torrie, G. M.; Valleau, J. P. Nonphysical Sampling Distributions in Monte Carlo Free-Energy Estimation: Umbrella Sampling. *J. Comput. Phys.* **1977**, *23*, 187–199.

[4] Kumar, S.; Rosenberg, J. M.; Bouzida, D.; Swendsen, R. H.; Kollman, P. A. The Weighted Histogram Analysis Method for Free-Energy Calculations on Biomolecules. I. The Method. *J. Comput. Chem.* **1992**, *13*, 1011–1021.

[5] Shirts, M. R.; Chodera, J. D. Statistically Optimal Analysis of Samples from Multiple Equilibrium States. *J. Chem. Phys.* **2008**, *129*, 124105.

[6] Tamai, Y. Delocalization boosts charge separation in organic solar cells. *Polym. J.* **2020**, *52*, 691–700.

[7] Hernandez, V.; Castiglioni, C.; Del Zoppo, M.; Zerbi, G. Confinement potential and π-electron delocalization in polyconjugated organic materials. *Phys. Rev. B* **1994**, *50*, 9815–9823.

[8] Lupton, J. M. Chromophores in Conjugated Polymers — All Straight? *ChemPhysChem* **2012**, *13*, 901–907.

[9] Troisi, A.; Shaw, A. Very Large π-Conjugation Despite Strong Nonplanarity: A Path for Designing New Semiconducting Polymers. *J. Phys. Chem. Lett.* **2016**, *7*, 4689–4694.

[10] Kleinschmidt, A. T.; Chen, A. X.; Ramji, R. S.; Pascal, T. A.; Lipomi, D. J. Decoupling Planarizing and Steric Energetics to Accurately Model the Rigidity of π-Conjugated Polymers. *J. Phys. Chem. B* **2023**, *127*, 2092–2102.

[11] Galuska, L. A.; McNutt, W. W.; Qian, Z.; Zhang, S.; Weller, D. W.; Dhakal, S.; King, E. R.;

Morgan, S. E.; Azoulay, J. D.; Mei, J. Impact of Backbone Rigidity on the Thermomechanical Properties of Semiconducting Polymers with Conjugation Break Spacers. *Macromolecules* **2020**, *53*, 6032–6042.

[12] Hu, Z.; Liu, J.; Simón-Bower, L.; Zhai, L.; Gesquiere, A. J. Influence of Backbone Rigidness on Single Chain Conformation of Thiophene-Based Conjugated Polymers. *J. Phys. Chem. B* **2013**, *117*, 4461–4467.

[13] Reid, D. R.; Jackson, N. E.; Bourque, A. J.; Snyder, C. R.; Jones, R. L.; de Pablo, J. J. Aggregation and Solubility of a Model Conjugated Donor–Acceptor Polymer. *J. Phys. Chem. Lett.* **2018**, *9*, 4802–4807.

[14] Wolf, C. M.; Kanekal, K. H.; Yimer, Y. Y.; Tyagi, M.; Omar-Diallo, S.; Pakhnyuk, V.; Luscombe, C. K.; Pfaendtner, J.; Pozzo, D. L. Assessment of molecular dynamics simulations for amorphous poly(3-hexylthiophene) using neutron and X-ray scattering experiments. *Soft Matter* **2019**, *15*, 5067–5083.

[15] Jackson, N. E.; Kohlstedt, K. L.; Savoie, B. M.; Olvera de la Cruz, M.; Schatz, G. C.; Chen, L. X.; Ratner, M. A. Conformational Order in Aggregates of Conjugated Polymers. *J. Am. Chem. Soc.* **2015**, *137*, 6254–6262.

[16] DuBay, K. H.; Hall, M. L.; Hughes, T. F.; Wu, C.; Reichman, D. R.; Friesner, R. A. Accurate Force Field Development for Modeling Conjugated Polymers. *J. Chem. Theory Comput.* **2012**, *8*, 4556–4569.

[17] Marcon, V.; Raos, G. Free Energies of Molecular Crystal Surfaces by Computer Simulation: Application to Tetrathiophene. *J. Am. Chem. Soc.* **2006**, *128*, 1408–1409.

[18] Raos, G.; Famulari, A.; Marcon, V. Computational reinvestigation of the bithiophene torsion potential. *Chem. Phys. Lett.* **2003**, *379*, 364–372.

[19] Jackson, N. E.; Savoie, B. M.; Kohlstedt, K. L.; Olvera de la Cruz, M.; Schatz, G. C.; Chen, L. X.; Ratner, M. A. Controlling Conformations of Conjugated Polymers and Small Molecules: The Role of Nonbonding Interactions. *J. Am. Chem. Soc.* **2013**, *135*, 10475–10483.

[20] Oh, J. T.; Ha, Y. H.; Kwon, S.-K.; Song, S.; Kim, J. Y.; Kim, Y.-H.; Choi, H. Twisted Linker Effect on Naphthalene Diimide-Based Dimer Electron Acceptors for Non-fullerene Organic Solar Cells. *Macromol. Rapid Commun.* **2018**, *39*, 1800108.

[21] Huang, Q.; Chen, J.; Yan, S.; Shao, X.; Dong, Y.; Liu, J.; Li, W.; Zhang, C. New Donor–Acceptor–Donor Conjugated Polymer with Twisted Donor–Acceptor Configuration for High-Capacitance Electrochromic Supercapacitor Application. *ACS Sustain. Chem. Eng.* **2021**, *9*, 13807–13817.

[22] Jorgensen, W. L.; Maxwell, D. S.; Tirado-Rives, J. Development and Testing of the OPLS All-Atom Force Field on Conformational Energetics and Properties of Organic Liquids. *J. Am. Chem. Soc.* **1996**, *118*, 11225–11236.

[23] Vanommeslaeghe, K.; Hatcher, E.; Acharya, C.; Kundu, S.; Zhong, S.; Shim, J.; Darian, E.; Guvench, O.; Lopes, P.; Vorobyov, I. CHARMM general force field: A force field for drug-like molecules compatible with the CHARMM all-atom additive biological force fields. *J. Comput. Chem.* **2010**, *31*, 671–690.

[24] Wang, J.; Wolf, R. M.; Caldwell, J. W.; Kollman, P. A.; Case, D. A. Development and testing of a general amber force field. *J. Comput. Chem.* **2004**, *25*, 1157–1174.

[25] Bonomi, M.; Bussi, G.; Camilloni, C.; Tribello, G. A.; Banáš, P.; Barducci, A.; Bernetti, M.; Bolhuis, P. G.; Bottaro, S.; Branduardi, D. Promoting transparency and reproducibility in enhanced molecular simulations. *Nat. Methods* **2019**, *16*, 670–673.

[26] Kleinschmidt, A. T.; Root, S. E.; Lipomi, D. J. Poly(3-hexylthiophene) (P3HT): fruit fly or outlier in organic solar cell research? *J. Mater. Chem. A* **2017**, *5*, 11396–11400.

[27] Zhang, Z.; Glotzer, S. C. Self-Assembly of Patchy Particles. *Nano Lett.* **2004**, *4*, 1407–1413.

[28] Dodda, L. S.; Cabeza de Vaca, I.; Tirado-Rives, J.; Jorgensen, W. L. LigParGen web server: an automatic OPLS-AA parameter generator for organic ligands. *Nucleic Acids Res.* **2017**, *45*, W331–W336.

[29] Shao, Y.; Gan, Z.; Epifanovsky, E.; Gilbert, A. T. B.; Wormit, M.; Kussmann, J.; Lange, A. W.; Behn, A.; Deng, J.; Feng, X.; Ghosh, D.; Goldey, M.; Horn, P. R.; Jacobson, L. D.; Kaliman, I.; Khaliullin, R. Z.; Kuś, T.; Landau, A.; Liu, J.; Proynov, E. I.; Rhee, Y. M.; Richard, R. M.; Rohrdanz, M. A.; Steele, R. P.; Sundstrom, E. J.; Woodcock, H. L., III; Zimmerman, P. M.; Zuev, D.; Albrecht, B.; Alguire, E.; Austin, B.; Beran, G. J. O.; Bernard, Y. A.; Berquist, E.; Brandhorst, K.; Bravaya, K. B.; Brown, S. T.; Casanova, D.; Chang, C.-M.; Chen, Y.; Chien, S. H.; Closser, K. D.; Crittenden, D. L.; Diedenhofen, M.; DiStasio, R. A., Jr.; Do, H.; Dutoi, A. D.; Edgar, R. G.; Fatehi, S.; Fusti-Molnar, L.; Ghysels, A.; Golubeva-Zadorozhnaya, A.; Gomes, J.; Hanson-Heine, M. W. D.; Harbach, P. H. P.; Hauser, A. W.; Hohenstein, E. G.; Holden, Z. C.; Jagau, T.-C.; Ji, H.; Kaduk, B.; Khistyaev, K.; Kim, J.; Kim, J.; King, R. A.; Klunzinger, P.; Kosenkov, D.; Kowalczyk, T.; Krauter, C. M.; Lao, K. U.; Laurent, A. D.; Lawler, K. V.; Levchenko, S. V.; Lin, C. Y.; Liu, F.; Livshits, E.; Lochan, R. C.; Luenser, A.; Manohar, P.; Manzer, S. F.; Mao, S.-P.; Mardirossian, N.; Marenich, A. V.; Maurer, S. A.; Mayhall, N. J.; Neuscamman, E.; Oana, C. M.; Olivares-Amaya, R.; O'Neill, D. P.; Parkhill, J. A.; Perrine, T. M.; Peverati, R.; Prociuk, A.; Rehn, D. R.; Rosta, E.; Russ, N. J.; Sharada, S. M.; Sharma, S.; Small, D. W.; Sodt, A.; Stein, T.; Stück, D.; Su, Y.-C.; Thom, A. J. W.; Tsuchimochi, T.; Vanovschi, V.; Vogt, L.; Vydrov, O.; Wang, T.; Watson, M. A.; Wen-

zel, J.; White, A.; Williams, C. F.; Yang, J.; Yeganeh, S.; Yost, S. R.; You, Z.-Q.; Zhang, I. Y.; Zhang, X.; Zhao, Y.; Brooks, B. R.; Chan, G. K. L.; Chipman, D. M.; Cramer, C. J.; Goddard, W. A., III; Gordon, M. S.; Hehre, W. J.; Klamt, A.; Schaefer, H. F., III; Schmidt, M. W.; Sherrill, C. D.; Truhlar, D. G.; Warshel, A.; Xu, X.; Aspuru-Guzik, A.; Baer, R.; Bell, A. T.; Besley, N. A.; Chai, J.-D.; Dreuw, A.; Dunietz, B. D.; Furlani, T. R.; Gwaltney, S. R.; Hsu, C.-P.; Jung, Y.; Kong, J.; Lambrecht, D. S.; Liang, W.; Ochsenfeld, C.; Rassolov, V. A.; Slipchenko, L. V.; Subotnik, J. E.; Van Voorhis, T.; Herbert, J. M.; Krylov, A. I.; Gill, P. M. W.; Head-Gordon, M. Advances in molecular quantum chemistry contained in the Q-Chem 4 program package. *Mol. Phys.* **2015**, *113*, 184–215.

[30] Jorgensen, W. L.; Tirado-Rives, J. Potential energy functions for atomic-level simulations of water and organic and biomolecular systems. *Proc. Natl. Acad. Sci. U. S. A.* **2005**, *102*, 6665–6670.

[31] Dodda, L. S.; Vilseck, J. Z.; Tirado-Rives, J.; Jorgensen, W. L. 1.14*CM1A-LBCC: Localized Bond-Charge Corrected CM1A Charges for Condensed-Phase Simulations. *J. Phys. Chem. B* **2017**, *121*, 3864–3870.

[32] Matt, C.; Meyer, D. L.; Lombeck, F.; Sommer, M.; Biskup, T. TBT Entirely Dominates the Electronic Structure of the Conjugated Copolymer PCDTBT: Insights from Time-Resolved Electron Paramagnetic Resonance Spectroscopy. *Macromolecules* **2018**, *51*, 4341–4349.

[33] Martínez, L.; Andrade, R.; Birgin, E. G.; Martínez, J. M. PACKMOL: A package for building initial configurations for molecular dynamics simulations. *J. Comput. Chem.* **2009**, *30*, 2157–2164.

[34] Thompson, A. P.; Aktulga, H. M.; Berger, R.; Bolintineanu, D. S.; Brown, W. M.; Crozier, P. S.; in't Veld, P. J.; Kohlmeyer, A.; Moore, S. G.; Nguyen, T. D.; Shan, R.; Stevens, M. J.; Tranchida, J.; Trott, C.; Plimpton, S. J. LAMMPS - a flexible simulation tool for particle-based materials modeling at the atomic, meso, and continuum scales. *Comput. Phys. Commun.* **2022**, *271*, 108171.

[35] Hockney, R. W.; Eastwood, J. W. *Computer simulation using particles*; Hilger: Bristol, 1988.

[36] Tuckerman, M. E.; Alejandre, J.; López-Rendón, R.; Jochim, A. L.; Martyna, G. J. A Liouville-operator derived measure-preserving integrator for molecular dynamics simulations in the isothermal–isobaric ensemble. *J. Phys. A: Math. Gen.* **2006**, *39*, 5629.

[37] Geuenich, D.; Hess, K.; Köhler, F.; Herges, R. Anisotropy of the Induced Current Density (ACID), a General Method To Quantify and Visualize Electronic Delocalization. *Chem. Rev.* **2005**, *105*, 3758–3772.

[38] Frisch, M. J.; Trucks, G. W.; Schlegel, H. B.; Scuseria, G. E.; Robb, M. A.; Cheeseman, J. R.; Scalmani, G.; Barone, V.; Petersson, G. A.; Nakatsuji, H. Gaussian 16 Revision C.01. Gaussian, Inc., Wallingford CT, 2016.

[39] Lu, T.; Chen, Q. A simple method of identifying π orbitals for non-planar systems and a protocol of studying π electronic structure. *Theor. Chem. Acc.* **2020**, *139*, 25.

[40] Kang, H.; Lee, Y.; Lee, G. H.; Chung, J. W.; Kwon, Y.-N.; Kim, J.-Y.; Kuzumoto, Y.; Gam, S.; Kang, S.-G.; Jung, J. Y. Strain-Tolerant, High-Detectivity, and Intrinsically Stretchable All-Polymer Photodiodes. *Adv. Funct. Mater.* **2023**, *33*, 2212219.

[41] Rosas Villalva, D.; Singh, S.; Galuska, L. A.; Sharma, A.; Han, J.; Liu, J.; Haque, M. A.; Jang, S.; Emwas, A. H.; Koster, L. J. A. Backbone-driven host–dopant miscibility modulates molecular doping in NDI conjugated polymers. *Mater. Horiz.* **2022**, *9*, 500–508.

[42] Weinhold, F. In *Encyclopedia of Computational Chemistry*; Schleyer, P. V. R., Allinger, N. L., Clark, T., Gasteiger, J., Kollman, P. A., Schaefer, H. F., Eds.; John Wiley & Sons: Chichester, UK, 1998; Vol. 3; pp 1792–1811.

[43] Poater, J.; Duran, M.; Solà, M.; Silvi, B. Theoretical Evaluation of Electron Delocalization in Aromatic Molecules by Means of Atoms in Molecules (AIM) and Electron Localization Function (ELF) Topological Approaches. *Chem. Rev.* **2005**, *105*, 3911–3947.

[44] Pipek, J.; Mezey, P. G. Dependence of MO shapes on a continuous measure of delocalization. *Int. J. Quantum Chem.* **1988**, *22*, 1–13.

[45] Pipek, J.; Mezey, P. G. A fast intrinsic localization procedure applicable for ab initio and semiempirical linear combination of atomic orbital wave functions. *J. Chem. Phys.* **1989**, *90*, 4916–4926.

[46] Reed, A. E.; Weinhold, F. Natural localized molecular orbitals. *J. Chem. Phys.* **1985**, *83*, 1736–1740.

[47] Edmiston, C.; Ruedenberg, K. Localized atomic and molecular orbitals. *Rev. Mod. Phys.* **1963**, *35*, 457–465.

[48] Shu, Y.; Lin, X.; Qin, H.; Hu, Z.; Jin, Y.; Peng, X. Quantum Dots for Display Applications. *Angew. Chem. Int. Ed.* **2020**, *59*, 22312.

[49] Kagan, C. R.; Lifshitz, E.; Sargent, E. H.; Talapin, D. V. Building devices from colloidal quantum dots. *Science* **2016**, *353*, aac5523.

[50] Alivisatos, A. P. Semiconductor Clusters, Nanocrystals, and Quantum Dots. *Science* **1996**, *271*, 933.

[51] Kim, J.; Roh, J.; Park, M.; Lee, C. Recent Advances and Challenges of Colloidal Quantum Dot Light-Emitting Diodes for Display Applications. *Adv. Mater.* **2024**, *36*, 2212220.

[52] Wang, Y.; Fedin, I.; Zhang, H.; Talapin, D. V. Direct optical lithography of functional inorganic nanomaterials. *Science* **2017**, *357*, 385.

[53] Park, S. Y.; Lee, S.; Yang, J.; Kang, M. S. Patterning Quantum Dots via Photolithography: A Review. *Adv. Mater.* **2023**, *35*, 2300546.

[54] Yang, J.; Hahm, D.; Kim, K.; Rhee, S.; Lee, M.; Kim, S.; Chang, J. H.; Park, H. W.; Lim, J.; Lee, M.; Kim, H.; Bang, J.; Ahn, H.; Cho, J. H.; Kwak, J.; Kim, B.; Lee, C.; Bae, W. K.; Kang, M. S. High-resolution patterning of colloidal quantum dots via non-destructive, light-driven ligand crosslinking. *Nat. Commun.* **2020**, *11*, 2874.

[55] Yang, J.; Lee, M.; Park, S. Y.; Park, M.; Kim, J.; Sitapure, N.; Hahm, D.; Rhee, S.; Lee, D.; Jo, H.; Jo, Y. H.; Lim, J.; Kim, J.; Shin, T. J.; Lee, D. C.; Kwak, K.; Kwon, J. S.; Kim, B.; Bae, W. K.; Kang, M. S. Nondestructive Photopatterning of Heavy-Metal-Free Quantum Dots. *Adv. Mater.* **2022**, *34*, 2205504.

[56] Lu, S.; Fu, Z.; Li, F.; Weng, K.; Zhou, L.; Zhang, L.; Yang, Y.; Qiu, H.; Liu, D.; Qing, W.; Ding, H.; Sheng, X.; Chen, M.; Tang, X.; Duan, L.; Liu, W.; Wu, L.; Yang, Y.; Zhang, H.; Li, J. Beyond a Linker: The Role of Photochemistry of Crosslinkers in the Direct Optical Patterning of Colloidal Nanocrystals. *Angew. Chem. Int. Ed.* **2022**, *61*, e202202633.

[57] Hahm, D.; Lim, J.; Kim, H.; Shin, J.-W.; Hwang, S.; Rhee, S.; Chang, J. H.; Yang, J.; Lim, C. H.; Jo, H.; Choi, B.; Cho, N. S.; Park, Y.-S.; Lee, D. C.; Hwang, E.; Chung, S.; Kang, C.-m.; Kang, M. S.; Bae, W. K. Direct patterning of colloidal quantum dots with adaptable dual-ligand surface. *Nat. Nanotechnol.* **2022**, *17*, 952.

[58] Lee, J.; Yeon, S.; Koo, B.; Sohn, B.; Park, S. J.; Kim, C.; Cho, H. Photocleavable Ligand-Induced Direct Photolithography of InP-Based Quantum Dots. *ACS Energy Lett.* **2025**, *10*, 94.

[59] Lim, J.; Bae, W. K.; Lee, D.; Nam, M. K.; Jung, J.; Lee, C.; Char, K.; Lee, S. InP@ZnSeS, Core@Composition Gradient Shell Quantum Dots with Enhanced Stability. *Chem. Mater.* **2011**, *23*, 4459.

[60] Lim, J.; Park, M.; Bae, W. K.; Lee, D.; Lee, S.; Lee, C.; Char, K. Highly Efficient Cadmium-Free Quantum Dot Light-Emitting Diodes Enabled by the Direct Formation of Excitons within InP@ZnSeS Quantum Dots. *ACS Nano* **2013**, *7*, 9019.

[61] Hanwell, M. D.; Curtis, D. E.; Lonie, D. C.; Vandermeersch, T.; Zurek, E.; Hutchison, G. R. Avogadro: an advanced semantic chemical editor, visualization, and analysis platform. *J. Cheminform.* **2012**, *4*, 17.

[62] O'Boyle, N. M.; Banck, M.; James, C. A.; Morley, C.; Vandermeersch, T.; Hutchison, G. R. Open Babel: An open chemical toolbox. *J. Cheminform.* **2011**, *3*, 33.

[63] Mayo, S. L.; Olafson, B. D.; Goddard, W. A. DREIDING: a generic force field for molecular simulations. *J. Phys. Chem.* **1990**, *94*, 8897.

[64] Dumbgen, K. C.; Pascazio, R.; van Beek, B.; Hens, Z.; Infante, I. Classical Force Field Parameters for InP and InAs Quantum Dots with Various Surface Passivations. *J. Phys. Chem. A* **2023**, *127*, 3427.

[65] Cosseddu, S.; Infante, I. Force Field Parametrization of Colloidal CdSe Nanocrystals Using an Adaptive Rate Monte Carlo Optimization Algorithm. *J. Chem. Theory Comput.* **2017**, *13*, 297.

[66] Sluydts, M.; De Nolf, K.; Van Speybroeck, V.; Cottenier, S.; Hens, Z. Ligand Addition Energies and the Stoichiometry of Colloidal Nanocrystals. *ACS Nano* **2016**, *10*, 1462.

[67] Wang, Z.; Wang, S.; Liu, Z.; Zhou, B.; Wen, Y.; Lu, Z.; Chen, R.; Shan, B. Bonding behavior and passivation mechanism of organic ligands (-SH, -NH2, -COOH) on ZnS (10-10) surface from first-principles calculations. *Appl. Surf. Sci.* **2021**, *545*, 148970.

[68] Ko, J.-H.; Yoo, D.; Kim, Y.-H. Atomic models for anionic ligand passivation of cation-rich surfaces of IV-VI, II-VI, and III-V colloidal quantum dots. *Chem. Commun.* **2017**, *53*, 388.

[69] Giannozzi, P.; Baroni, S.; Bonini, N.; Calandra, M.; Car, R.; Cavazzoni, C.; Ceresoli, D.; Chiarotti, G. L.; Cococcioni, M.; Dabo, I.; Dal Corso, A.; de Gironcoli, S.; Fabris, S.; Fratesi, G.; Gebauer, R.; Gerstmann, U.; Gougoussis, C.; Kokalj, A.; Lazzeri, M.; Martin-Samos, L.; Marzari, N.; Mauri, F.; Mazzarello, R.; Paolini, S.; Pasquarello, A.; Paulatto, L.; Sbraccia, C.; Scandolo, S.; Sclauzero, G.; Seitsonen, A. P.; Smogunov, A.; Umari, P.; Wentzcovitch, R. M. QUANTUM ESPRESSO: a modular and open-source software project for quantum simulations of materials. *J. Phys.: Condens. Matter* **2009**, *21*, 395502.

[70] Giannozzi, P.; Andreussi, O.; Brumme, T.; Bunau, O.; Buongiorno Nardelli, M.; Calandra, M.; Car, R.; Cavazzoni, C.; Ceresoli, D.; Cococcioni, M.; Colonna, N.; Carnimeo, I.; Dal Corso, A.; de Gironcoli, S.; Delugas, P.; DiStasio, R. A.; Ferretti, A.; Floris, A.; Fratesi, G.; Fugallo, G.; Gebauer, R.; Gerstmann, U.; Giustino, F.; Gorni, T.; Jia, J.; Kawamura, M.; Ko, H. Y.; Kokalj, A.; Kucukbenli, E.; Lazzeri, M.; Marsili, M.; Marzari, N.; Mauri, F.; Nguyen, N. L.; Nguyen, H. V.; Otero-de-la Roza, A.; Paulatto, L.; Ponce, S.; Rocca, D.; Sabatini, R.; Santra, B.; Schlipf, M.; Seitsonen, A. P.; Smogunov, A.; Timrov, I.; Thonhauser, T.; Umari, P.; Vast, N.; Wu, X.; Baroni, S. Advanced capabilities for materials modelling with Quantum ESPRESSO. *J. Phys.: Condens. Matter* **2017**, *29*, 465901.

[71] Perdew, J. P.; Burke, K.; Ernzerhof, M. Generalized Gradient Approximation Made Simple. *Phys. Rev. Lett.* **1996**, *77*, 3865.

[72] Vanderbilt, D. Soft self-consistent pseudopotentials in a generalized eigenvalue formalism. *Phys. Rev. B* **1990**, *41*, 7892.

[73] Prandini, G.; Marrazzo, A.; Castelli, I. E.; Mounet, N.; Marzari, N. Precision and efficiency in solid-state pseudopotential calculations. *npj Comput. Mater.* **2018**, *4*, 72.

[74] Thompson, A. P.; Aktulga, H. M.; Berger, R.; Bolintineanu, D. S.; Brown, W. M.; Crozier, P. S.; in 't Veld, P. J.; Kohlmeyer, A.; Moore, S. G.; Nguyen, T. D.; Shan, R.; Stevens, M. J.; Tranchida, J.; Trott, C.; Plimpton, S. J. LAMMPS - a flexible simulation tool for particle-based materials modeling at the atomic, meso, and continuum scales. *Comput. Phys. Commun.* **2022**, *271*, 108171.

[75] Shinoda, W.; Shiga, M.; Mikami, M. Rapid estimation of elastic constants by molecular dynamics simulation under constant stress. *Phys. Rev. B* **2004**, *69*, 134103.

[76] Martyna, G. J.; Tobias, D. J.; Klein, M. L. Constant pressure molecular dynamics algorithms. *J. Chem. Phys.* **1994**, *101*, 4177.

[77] Parrinello, M.; Rahman, A. Polymorphic transitions in single crystals: A new molecular dynamics method. *J. Appl. Phys.* **1981**, *52*, 7182.

[78] Tuckerman, M. E.; Alejandre, J.; Lopez-Rendon, R.; Jochim, A. L.; Martyna, G. J. A Liouville-operator derived measure-preserving integrator for molecular dynamics simulations in the isothermal-isobaric ensemble. *J. Phys. A: Math. Gen.* **2006**, *39*, 5629.

[79] Li, C.; Strachan, A. Molecular simulations of crosslinking process of thermosetting polymers. *Polymer* **2010**, *51*, 6058.

[80] Hossain, D.; Tschopp, M. A.; Ward, D. K.; Bouvard, J. L.; Wang, P.; Horstemeyer, M. F. Molecular dynamics simulations of deformation mechanisms of amorphous polyethylene. *Polymer* **2010**, *51*, 6071.

[81] Shirts, M. R.; Klein, C.; Swails, J. M.; Yin, J.; Gilson, M. K.; Mobley, D. L.; Case, D. A.; Zhong, E. D. Lessons learned from comparing molecular dynamics engines on the SAMPL5 dataset. *J. Comput.-Aided Mol. Des.* **2017**, *31*, 147.

[82] Michaud-Agrawal, N.; Denning, E. J.; Woolf, T. B.; Beckstein, O. MDAnalysis: A toolkit for the analysis of molecular dynamics simulations. *J. Comput. Chem.* **2011**, *32*, 2319.

[83] Lorenz, C. D.; May, R.; Ziff, R. M. Similarity of Percolation Thresholds on the HCP and FCC Lattices. *J. Stat. Phys.* **2000**, *98*, 961.

[84] Elghanian, R.; Storhoff, J. J.; Mucic, R. C.; Letsinger, R. L.; Mirkin, C. A. Selective Colorimetric Detection of Polynucleotides Based on the Distance-Dependent Optical Properties of Gold Nanoparticles. *Science* **1997**, *277*, 1078–1081.

[85] Dreaden, E. C.; Alkilany, A. M.; Huang, X.; Murphy, C. J.; El-Sayed, M. A. The Golden Age: Gold Nanoparticles for Biomedicine. *Chem. Soc. Rev.* **2012**, *41*, 2740–2779.

[86] Boisselier, E.; Astruc, D. Gold Nanoparticles in Nanomedicine: Preparations, Imaging, Diagnostics, Therapies and Toxicity. *Chem. Soc. Rev.* **2009**, *38*, 1759–1782.

[87] Jin, Z.; Mantri, Y.; Retout, M.; Cheng, Y.; Zhou, J.; Jorns, A.; Fajtová, P.; Yim, W.; Moore, C.; Xu, M.; Creyer, M. N.; Borum, R. M.; Zhou, J.; Wu, Z.; He, T.; Penny, W. F.; O'Donoghue, A. J.; Jokerst, J. V. A Charge-Switchable Zwitterionic Peptide for Rapid Detection of SARS-CoV-2 Main Protease. *Angew. Chem. Int. Ed.* **2022**, *61*, e202112995.

[88] Liu, J.; Lu, Y. A Colorimetric Lead Biosensor Using DNAzyme-Directed Assembly of Gold Nanoparticles. *J. Am. Chem. Soc.* **2003**, *125*, 6642–6643.

[89] Aldewachi, H.; Chalati, T.; Woodroofe, M. N.; Bricklebank, N.; Sharrack, B.; Gardiner, P. Gold Nanoparticle-Based Colorimetric Biosensors. *Nanoscale* **2018**, *10*, 18–33.

[90] Chang, C.-C.; Chen, C.-P.; Wu, T.-H.; Yang, C.-H.; Lin, C.-W.; Chen, C.-Y. Gold Nanoparticle-Based Colorimetric Strategies for Chemical and Biological Sensing Applications. *Nanomaterials* **2019**, *9*, 861.

[91] Zhao, W.; Chiuman, W.; Lam, J. C. F.; McManus, S. A.; Chen, W.; Cui, Y.; Pelton, R.; Brook, M. A.; Li, Y. DNA Aptamer Folding on Gold Nanoparticles: From Colloid Chemistry to Biosensors. *J. Am. Chem. Soc.* **2008**, *130*, 3610–3618.

[92] Stevens, M. M.; Flynn, N. T.; Wang, C.; Tirrell, D. A.; Langer, R. Coiled-Coil Peptide-Based Assembly of Gold Nanoparticles. *Adv. Mater.* **2004**, *16*, 915–918.

[93] Retout, M.; Jin, Z.; Tsujimoto, J.; Mantri, Y.; Borum, R.; Creyer, M. N.; Yim, W.; He, T.; Chang, Y.-C.; Jokerst, J. V. Di-Arginine Additives for Dissociation of Gold Nanoparticle Aggregates: A Matrix-Insensitive Approach with Applications in Protease Detection. *ACS Appl. Mater. Interfaces* **2022**, *14*, 52553–52565.

[94] Aili, D.; Enander, K.; Rydberg, J.; Inganäs, I.; Liedberg, B. Tunable Assembly of Peptide-Coated Gold Nanoparticles. *Plasmonics* **2007**, *2*, 119–127.

[95] Lam, B.; Ramji, R.; Mullooly, M.; Closser, K. D.; Pascal, T. A.; Jokerst, J. V. Mechanism of Cationic Peptide-Induced Assembly of Gold Nanoparticles: Modulation of Electrostatic Repulsion. *Aggregate* **2026**, e70043.

[96] Monti, S.; Barcaro, G.; Sementa, L.; Carravetta, V.; Ågren, H. Characterization of the Adsorption Dynamics of Trisodium Citrate on Gold in Water Solution. *RSC Adv.* **2017**, *7*, 49655–49663.

[97] Chong, G.; Laudadio, E. D.; Wu, M.; Murphy, C. J.; Hamers, R. J.; Hernandez, R. Density, Structure, and Stability of $Citrate^{3-}$ and $H_2citrate^{-}$ on Bare and Coated Gold Nanoparticles. *J. Phys. Chem. C* **2018**, *122*, 28393–28404.

[98] Al-Johani, H.; Abou-Hamad, E.; Jedidi, A.; Widdifield, C. M.; Viger-Gravel, J.; Sangaru, S. S.; Gajan, D.; Anjum, D. H.; Ould-Chikh, S.; Hedhili, M. N.; Gurinov, A.; Kelly, M. J.; El Eter, M.; Cavallo, L.; Emsley, L.; Basset, J.-M. The Structure and Binding Mode of Citrate in the Stabilization of Gold Nanoparticles. *Nat. Chem.* **2017**, *9*, 890–895.

[99] Wright, L. B.; Rodger, P. M.; Walsh, T. R. Aqueous Citrate: A First-Principles and Force-Field Molecular Dynamics Study. *RSC Adv.* **2013**, *3*, 16399–16409.

[100] Salassi, S.; Caselli, L.; Cardellini, J.; Lavagna, E.; Montis, C.; Berti, D.; Rossi, G. A Martini Coarse Grained Model of Citrate-Capped Gold Nanoparticles Interacting with Lipid Bilayers. *J. Chem. Theory Comput.* **2021**, *17*, 6597–6609.

[101] Janitra, R. S.; Destiarani, W.; Hardianto, A.; Baroroh, U.; Rohmatulloh, F. G.; Rustaman; Subroto, T.; Rukiah; Yusuf, M. Multilayer Model of Gold Nanoparticles (AuNPs) and Its Application in the Classical Molecular Dynamics Simulation of Citrate-Capped AuNPs. *J. Phys. Chem. B* **2023**, *127*, 7103–7110.

[102] Chong, G.; Hernandez, R. Adsorption Dynamics and Structure of Polycations on Citrate-Coated Gold Nanoparticles. *J. Phys. Chem. C* **2018**, *122*, 19962–19969.

[103] Petretto, E.; Campomanes, P.; Vanni, S. Development of a Coarse-Grained Model for Surface-Functionalized Gold Nanoparticles: Towards an Accurate Description of Their Aggregation Behavior. *Soft Matter* **2023**, *19*, 3290–3300.

[104] Kim, T.; Lee, K.; Gong, M.-S.; Joo, S.-W. Kinetics of Gold Nanoparticle Aggregation: Experiments and Modeling. *J. Colloid Interface Sci.* **2008**, *318*, 238–243.

[105] Lin, J.-Q.; Zhang, H.-W.; Chen, Z.; Zheng, Y.-G.; Zhang, Z.-Q.; Ye, H.-F. Simulation Study of Aggregations of Monolayer-Protected Gold Nanoparticles in Solvents. *J. Phys. Chem. C* **2011**, *115*, 18991–18998.

[106] Yim, W.; Retout, M.; Chen, A. A.; Ling, C.; Amer, L.; Jin, Z.; Chang, Y.-C.; Chavez, S.; Barrios, K.; Lam, B.; Li, Z.; Zhou, J.; Shi, L.; Pascal, T. A.; Jokerst, J. V. Goldilocks Energy Minimum: Peptide-Based Reversible Aggregation and Biosensing. *ACS Appl. Mater. Interfaces* **2023**, *15*, 42293–42303.

[107] Plimpton, S. J.; Pollock, R.; Stevens, M. Particle-Mesh Ewald and rRESPA for Parallel Molecular Dynamics Simulations. Proceedings of the Eighth SIAM Conference on Parallel Processing for Scientific Computing. Minneapolis, MN, 1997.

[108] Brooks, B. R.; Bruccoleri, R. E.; Olafson, B. D.; States, D. J.; Swaminathan, S.; Karplus, M. CHARMM: A Program for Macromolecular Energy, Minimization, and Dynamics Calculations. *J. Comput. Chem.* **1983**, *4*, 187–217.

[109] Ryckaert, J.-P.; Ciccotti, G.; Berendsen, H. J. C. Numerical Integration of the Cartesian Equations of Motion of a System with Constraints: Molecular Dynamics of n-Alkanes. *J. Comput. Phys.* **1977**, *23*, 327–341.

[110] Nosé, S. A Unified Formulation of the Constant Temperature Molecular Dynamics Methods. *J. Chem. Phys.* **1984**, *81*, 511–519.

[111] Hoover, W. G. Canonical Dynamics: Equilibrium Phase-Space Distributions. *Phys. Rev. A* **1985**, *31*, 1695–1697.

[112] Heinz, H.; Vaia, R. A.; Farmer, B. L.; Naik, R. R. Accurate Simulation of Surfaces and Interfaces of Face-Centered Cubic Metals Using 12-6 and 9-6 Lennard-Jones Potentials. *J. Phys. Chem. C* **2008**, *112*, 17281–17290.

[113] Hanwell, M. D.; others Avogadro: an advanced semantic chemical editor, visualization, and analysis platform. *J. Cheminform.* **2012**, *4*, 17.

[114] Bayly, C. I.; Cieplak, P.; Cornell, W. D.; Kollman, P. A. A Well-Behaved Electrostatic Potential Based Method Using Charge Restraints for Deriving Atomic Charges: The RESP Model. *J. Phys. Chem.* **1993**, *97*, 10269–10280.

[115] Improta, R.; Barone, V.; Scalmani, G.; Frisch, M. J. A State-Specific Polarizable Continuum Model Time Dependent Density Functional Theory Method for Excited State Calculations in Solution. *J. Chem. Phys.* **2006**, *125*, 054103.

[116] Wang, J.; Wang, W.; Kollman, P. A.; Case, D. A. Automatic Atom Type and Bond Type Perception in Molecular Mechanical Calculations. *J. Mol. Graphics Modell.* **2006**, *25*, 247–260.

[117] Jensen, K. P.; Jorgensen, W. L. Halide, Ammonium, and Alkali Metal Ion Parameters for Modeling Aqueous Solutions. *J. Chem. Theory Comput.* **2006**, *2*, 1499–1509.

[118] Tribello, G. A.; Bonomi, M.; Branduardi, D.; Camilloni, C.; Bussi, G. PLUMED 2: New Feathers for an Old Bird. *Comput. Phys. Commun.* **2014**, *185*, 604–613.

[119] Jarzynski, C. Nonequilibrium Equality for Free Energy Differences. *Phys. Rev. Lett.* **1997**,

78, 2690–2693.

[120] Michaud-Agrawal, N.; others MDAnalysis: A toolkit for the analysis of molecular dynamics simulations. *J. Comput. Chem.* **2011**, *32*, 2319.

[121] Gowers, R. J.; Linke, M.; Barnoud, J.; Reddy, T. J. E.; Melo, M. N.; Seyler, S. L.; Domański, J.; Dotson, D. L.; Buchoux, S.; Kenney, I. M.; Beckstein, O. MDAnalysis: A Python Package for the Rapid Analysis of Molecular Dynamics Simulations. Proceedings of the 15th Python in Science Conference. 2016; pp 98–105.

[122] Lam, B.; Ramji, R.; Mullooly, M.; Closser, K. D.; Pascal, T. A.; Jokerst, J. V. Electrostatic and Steric Forces Drive Reversible Aggregation of Gold Nanoparticles. *J. Phys. Chem. C* **2026**,